OSMOSE VOD data set documentation and analysis report

Simon Boitard, Arnaud Mialon, Nemesio Rodríguez-Fernández

OSMOSE
VOD data set documentation and analysis report
T4-D08 (TN #04)

Version : 1.0 (June 5, 2024)

Ref.: SO-TN-CB-GS-0118

OSMOSE
VOD data set documentation and analysis report
T4-D08 (TN #04)

CESBIO-SMOS report **SO-TN-CB-GS-0118**

Simon Boitard[1],Arnaud Mialon[1], Nemesio J. Rodríguez-Fernández[1]

[1] **CESBIO**
Université de Toulouse, CNES/CNRS/INRAE/IRD/UT3, 18, Avenue Edouard Belin, 31401 Toulouse, France

Release	Date	Details	Editors
1.0	02 April 2024	Initial document	Arnaud Mialon

Contact: Arnaud Mialon arnaud.mialon@univ-tlse3.fr

Contents

List of Figures

List of Tables

Acronyms

2S	Two Stream Radiative Transfer Model
AMSRE	Advanced Microwave Scanning Radiometer-EOS
AMSR2	Advanced Microwave Scanning Radiometer 2
ADF	Auxiliary Data File
ATBD	Algorithm Theoretical Baseline Document
CATDS	Centre Aval de Traitement des Données SMOS
CESBIO	Centre d'Etudes Spatiales de la Biosphère
DQX	Data Quality Index
EASE	Equal-Area Scalable Earth Grid
ECMWF	European Centre for Medium-range Weather Forecasting
IGBP	International Geosphere-Biosphere Programme
L-MEB	L - band Microwave Emission of the Biosphere
LSB / MSB	Lowest / Most Significant Bit *
MD	Cardioid Model
RFI	Radiometric Frequency Interference
RTM	Radiative Transfer Model
SM	Soil Moisture
SMOS	Soil Moisture and Ocean Salinity
Tau	Vegetation Optical thickness
TB	Brightness Temperature
VOD	Vegetation Optical Depth

1 Introduction

1.1 Purpose of the document

This technical document is the deliverable D08 of the ESA PM VOS OSMOSE project, contract No. 4000137990/22/NL/IA. It corresponds to task#4, and is the fourth technical report of the projet. Its purpose is to analyse the VOD produced by the OSMOSE processing chains at L, C and X bands.

1.2 Related documents

Table 1: Applicable documents

Id.	Ref.	Description
AD. 1	ESA-EOPSM-SMOS-SOW-3918	Statement of Work for the project "10 YEARS OF SMOS - PASSIVE MICROWAVE VEGETATION OPACITY STUDY (PM-VO-S).

1.3 Reference documents

Table 2: Reference documents

Id.	Ref.	Description
RD. 1	SO-TN-CB-GS-0116	VOD processing chain ATBD T2-D03 (TN#02)
RD. 2	SO-TN-CB-GS-0115	OSMOSE Database Manual Microwave T3-D06 (TN#03)
RD. 3	TN_PM-VO-S_WP1	Theoretical analysis of multi-frequency VOD and albedo (version 2)

2 VOD sensitivity analysis

To produce VOD from Brightness Temperatures (TB), the OSMOSE project capitalized on an existing algorithm for the L- band and adapted it to the C and X bands. The parametrized chain for the three frequencies is presented in the Algorithm Theoretical Basis Document (ATBD): **OSMOSE: VOD processing chain ATBD** (Deliverable 03 Task 02, Technical Note 2 of the OSMOSE project SO-TN-CB-GS-0116). In particular, Table 4 of the ATBD (see (3)) already introduced the parameters that were tested, to adapt the processing chain to C- and X-bands. The Table is displayed below (Table 3) with a reminder of the parameter significance.

Table 3: Tested parameters and associated values for tuning the retrieval platform per frequency band

Parameter	**Tested value**		
Band	**L**	**C**	**X**
RTM	LMEB or 2S	LMEB or 2S	LMEB or 2S
Hr	[0 0.15 0.3 0.4]	[0 0.15 0.3 0.4]	[0 0.15 0.3 0.4]
RFI filtering	[0.2 0.8]	N/A	N/A
ω	$\omega = f(TH)$	[0.01:0.01:0.15] $\omega = f(TH)$	[0.04 0.05 0.06 0.08]
Free parameters	VOD/SM VOD/ACard	VOD/SM VOD/ACard VOD only (SM from ERA5)	VOD/SM VOD/ACard VOD only (SM from ERA5)
Retrieval limits	Free or 0⩽SM⩽1 & 0⩽VOD⩽2	Free or 0⩽SM⩽1 & 0⩽VOD⩽2	Free or 0⩽SM⩽1 & 0⩽VOD⩽2
Veg. Temperature	Skin Temperature 2m Air Temperature	Skin Temperature 2m Air Temperature	Skin Temperature 2m Air Temperature

Here are some explanations of some tested parameters:

- *RFI filtering*: to assess the retrieval quality when applying different RFI filtering thresholds, for SMOS only. The L3TB impacted by RFI are filtered using the ratio Nb_RFI_Flags / Nviews, i.e. number of SMOS TB impacted by RFI over the number of TB, see (3). Two thresholds are tested, 0.2 being too restrictive removing too many TBs. A threshold of 0.8 allows us to deal with more TBs. It is justified as two more filters are applied on the VOD: removing VOD with an RMSE¿8K and outliers when computing the yearly average.
- ω: was already fine-tuned for the L-band MEB. Tests were carried out with a Tree Height (TH) dependent omega based on the results from WSL analyses ((24)). For C and X bands additional tests with fixed ω values were conducted.
- *Free parameters*: As it was unsure whether SM would be a relevant parameter for C and X-bands, some tests were conducted to retrieve VOD and ACard, instead of VOD and SM. ACARD is the cardioid model (19), which is a simple model to estimate the module of the dielectric constant. It can be used to characterize particular cases (frozen/bare soils) where the soil model (i.e. Mironov dielectric model) is not adapted. In the cases of X and C bands, we tested 2-parameter retrievals with ACard instead of the SM, as it was not evident that performing a SM/VOD retrieval would lead to satisfying results in terms of VOD and also in terms of RMSE (modeled TB model versus SMOS TB). Indeed, C and X is less sensitive to the soil in particular with a vegetation layer. Additionally, the retrieval of a single parameter (with SM from ERA5) versus the retrieval of two parameters was also tested.
- *Retrieval limits*: Assess the impact on the VOD, of constraining the free parameters in the cost function.

In the following section, we present the sensitivity of the VOD at X and C bands with respect to the various parameters, as described above.

2.1 Influence of the Radiative Transfer Model

In the frame of this project, two Radiative Transfer Models (RTM) have been tested:

- The L-band Microwave Emission of the Biosphere Model (LMEB) which uses the classical $\tau - \omega$ model (23)
- The Two-Stream Model (2S) which is able to simulate higher degrees of interaction between different layers (soil, vegetation, atmosphere) (18)

A test for the L-band was conducted over 1 month for both ascending and descending orbits and using both RTM. The ω value is converted from LMEB values to 2S values using Eq. 23 from (18). It means that the 2S model is not used per se, but is rather fitted into the LMEB. The values used for ω_{LMEB} are 0.06 over forest pixels and 0.1 over low vegetation pixels as recalled in (3). The output VOD were then averaged for each orbit type. One of the final purposes of the microwave part of the OSMOSE project is the estimation of the AGB from multi-frequency VOD. When conducting the sensitivity analysis of different parameters on the VOD, the spatial correlation of this averaged VOD with respect to the CCI AGB is a relevant indicator. In this study, the Pearson correlation coefficient (R) and Spearman correlation coefficient (Rho) are used. Fig. 1 shows the spatial density plot between the AGB from the CCI (17) and the 1-month average VOD for ascending and descending orbits using the 2S or the LMEB for the descending (top panel) or ascending orbits (bottom panel).

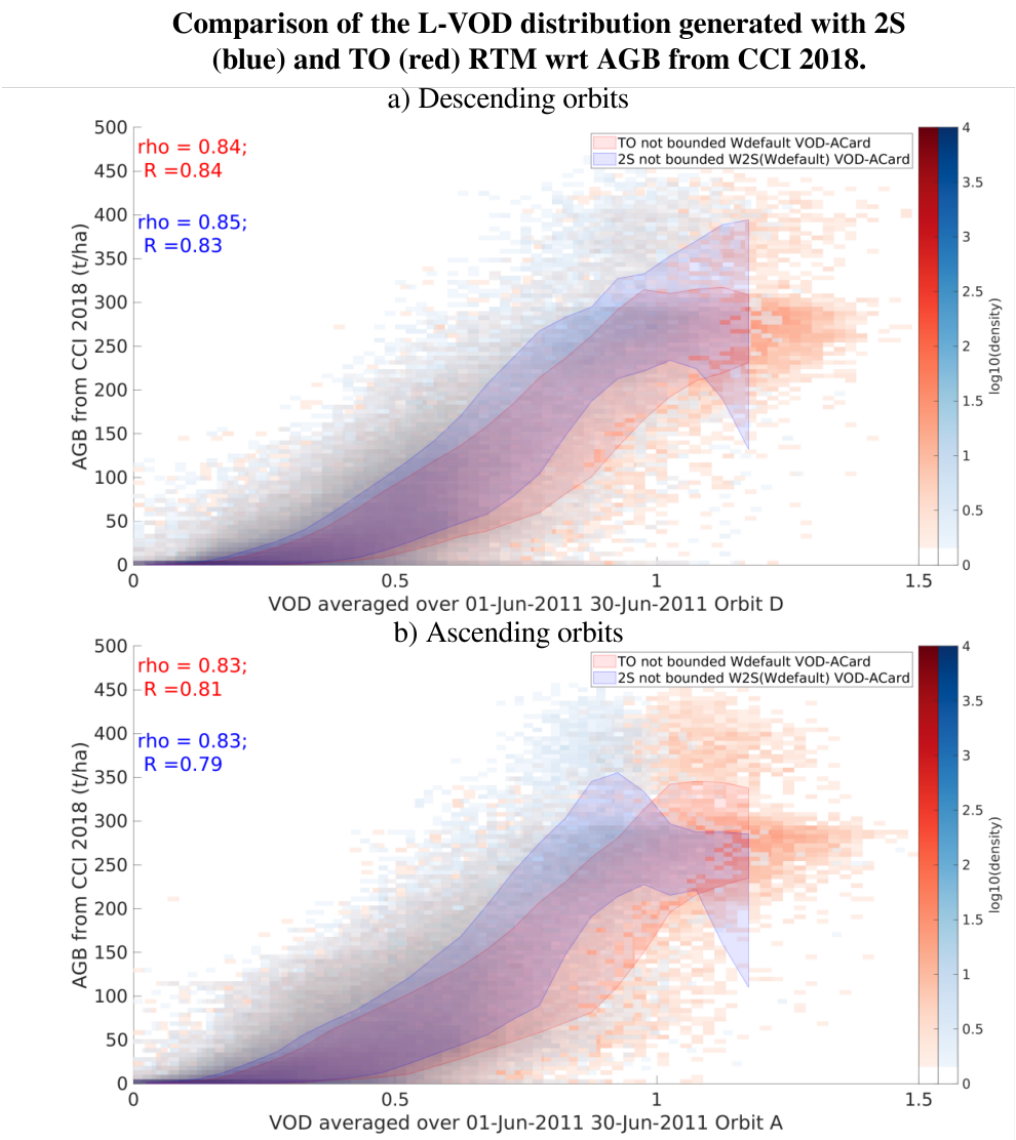

Figure 1: Density plot of the OSMOSE L-VOD for June 2011 against the AGB from CCI 2018. The red color refers to the use of the TO model to retrieve the VOD and the blue color refers to the use of the 2S model. In both cases, the couple (VOD/ACard) was retrieved, the retrieval was not constrained and the default values of ω were used (eq 23 of (18) was used to convert from TO to 2S value). The shaded areas correspond to the interval in-between quantiles 16 and 84 and contains 68% of the distribution. (a) for descending orbits and (b) for ascending orbits.

Fig. 1 shows that the RTM does not significantly impact the VOD correlation with the AGB for the L-band for both orbit types. In both cases, the 2S L-VOD saturates to a lower value than the TO L-VOD. The choice of the RTM does not greatly impact the distributions.

A similar test was conducted for C-band over July 2011. The ω value are derived from the MEMLV (outputs of OSMOSE WP1, WSL) and depends on the the TH. A map of the C-band omega for the TO RTM is displayed in Fig. 2. The ω values from TO were converted to 2S using Eq. (23) of (18). The results are displayed on Fig 3.

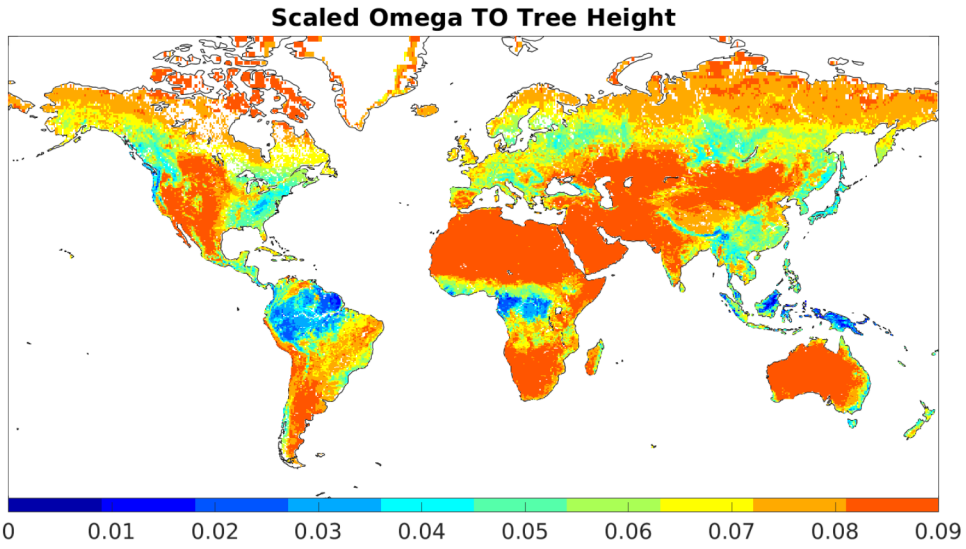

Figure 2: Map of ω for the C-band TO RTM based on the WSL Look-Up Tables

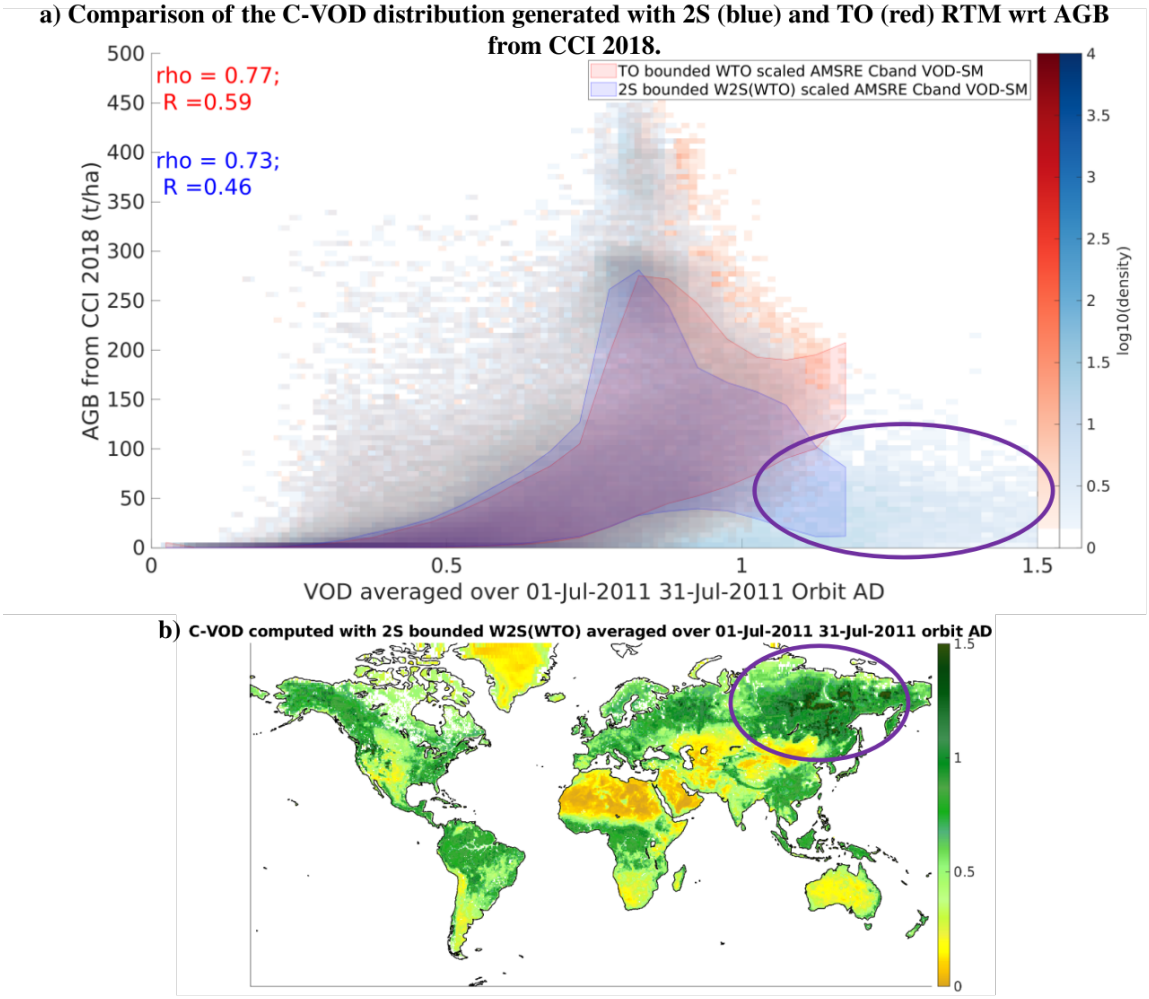

Figure 3: Density plot of the OSMOSE C-VOD for July 2011 against the AGB from CCI 2018. The red color refers to the use of the TO model to retrieve the VOD and the blue color refers to the use of the 2S model. In both cases, the couple (VOD/ACard) was retrieved, the retrieval was not constrained and the default values of ω were used (eq 23 of (18) was used to convert from TO to 2S value). The shaded areas correspond to the interval in-between quantiles 16 and 84 and contain 68% of the distribution.

With the 2S configuration, a significantly large area over Eastern Russia exhibits unexpected high VOD. This area is highlighted in purple on panel (a) of Fig. 3 and the corresponding points are also highlighted in purple on panel (b). These 2S VOD are higher than the VOD over the Tropics and do not seem realistic as they correspond to AGB values around 50-100 Mg ha^{-1}. The correlation also drops with the 2S RTM. Hence, the TO model seems to be better suited for the C-band. The same results apply to the X-band.

2.2 Influence of the retrieval parameters

The retrieval algorithm allows us to derive various parameters that drive the RTM, and the emission observed by the sensors. The most obvious ones are the SM or the dielectric constant for the soil layer, and the VOD for the vegetation layer, as described at the beginning of the section.

2.2.1 L-Band

For SMOS L-band, two couples of free parameters were tested:

- Retrieving (VOD, SM)
- Retrieving (VOD, ACard) and setting SM to the default initial value of 0.2 m^{-3}/m^{-3}

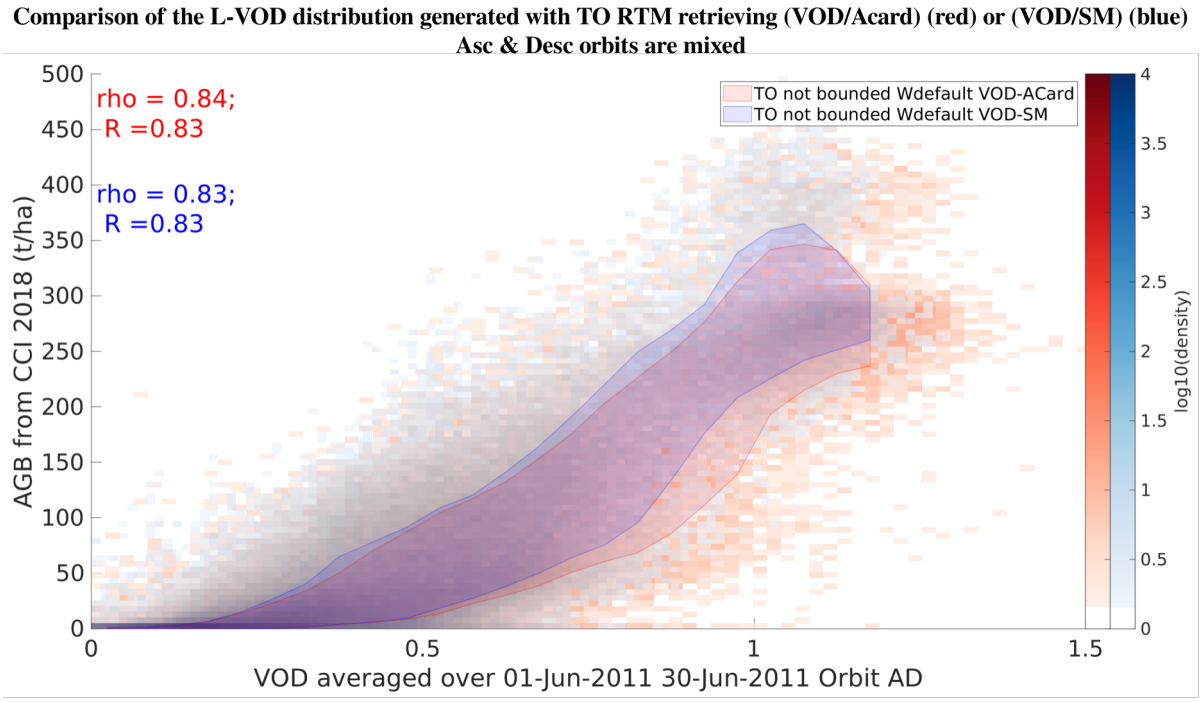

Figure 4: Density plot of the OSMOSE L-VOD for June 2011 against the AGB from CCI 2018. The red color refers to the retrieval of the (VOD/ACard) couple and the blue color to the (VOD-SM) couple. The TO retrieval was not constrained and the default values of ω were used. The shaded areas correspond to the interval in-between quantiles 16 and 84 and contains 68% of the distribution.

Fig. 4 shows that retrieving (VOD/ACard) or (VOD/SM) does not significantly impact the VOD correlation with the AGB from CCI 2018. It is not too surprising as the VOD are the pixel averaged over a month which probably smooths the small differences that may occur. The derived Acard is the dielectric constant, which is mainly driven by the SM at L-band. SM and Acard are in that case linked and lead to similar VOD. All correlation coefficients are around 0.83. The dispersion highlighted by the colored shaded area, is lower when using the classical (VOD/SM) couple. The (VOD/SM) couple is then considered in the OSMOSE processing chain for L-band.

2.2.2 C-Band

For the C-band, the same couples (VOD/SM or VOD/ACard) were tested out. As the observing frequency is higher than L-band, there was a possibility that the C-band observations were not sensitive to the ground underneath a vegetation layer, and that retrieving ACard would be more relevant than retrieving SM.

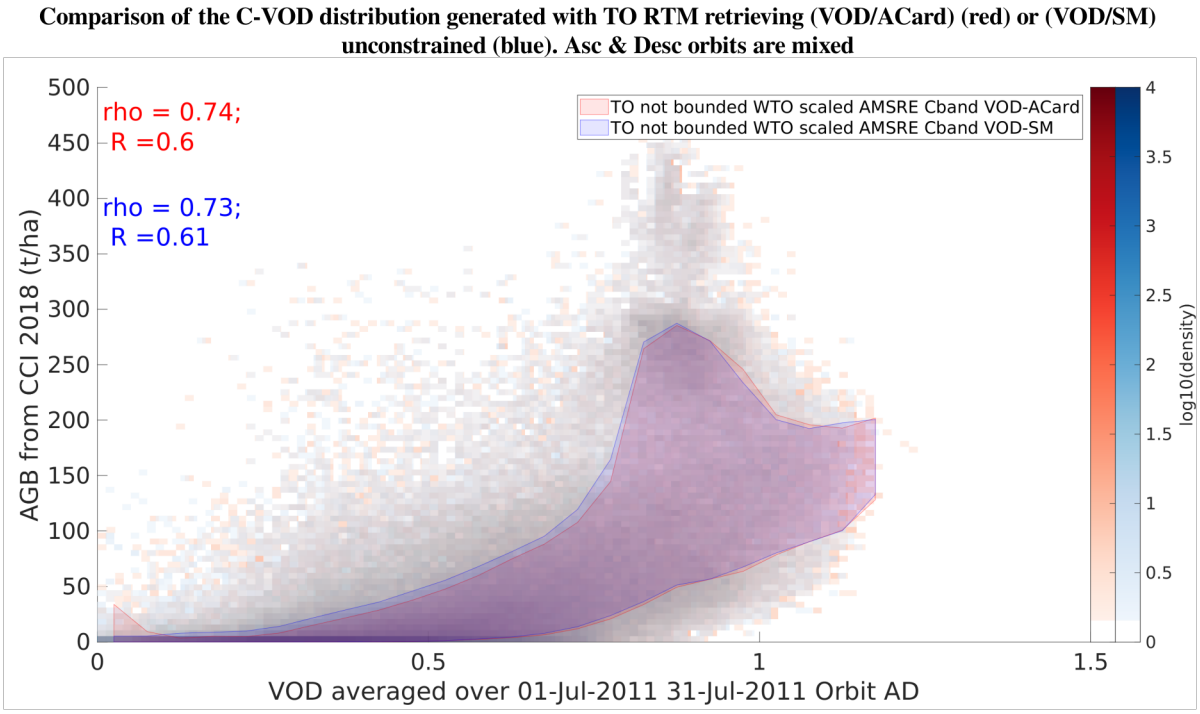

Figure 5: Density plot of the OSMOSE C-VOD for July 2011 against the AGB from CCI 2018. The red color refers to the retrieval of the (VOD/ACard) couple and the blue color to the (VOD-SM) couple. The TO retrieval was not constrained and the default values of ω were used. The shaded areas correspond to the interval in-between quantiles 16 and 84 and contains 68% of the distribution.

As shown on Fig. 5, like for L-band, retrieving Acard rather than SM does not impact the correlation of the VOD with the AGB from CCI 2018. (VOD/SM) will hence be retrieved for the C-band. This also ensures homogeneity with L-band retrieval.

2.3 Influence of constraining the retrieval with upper and lower boundaries

2.3.1 L-Band

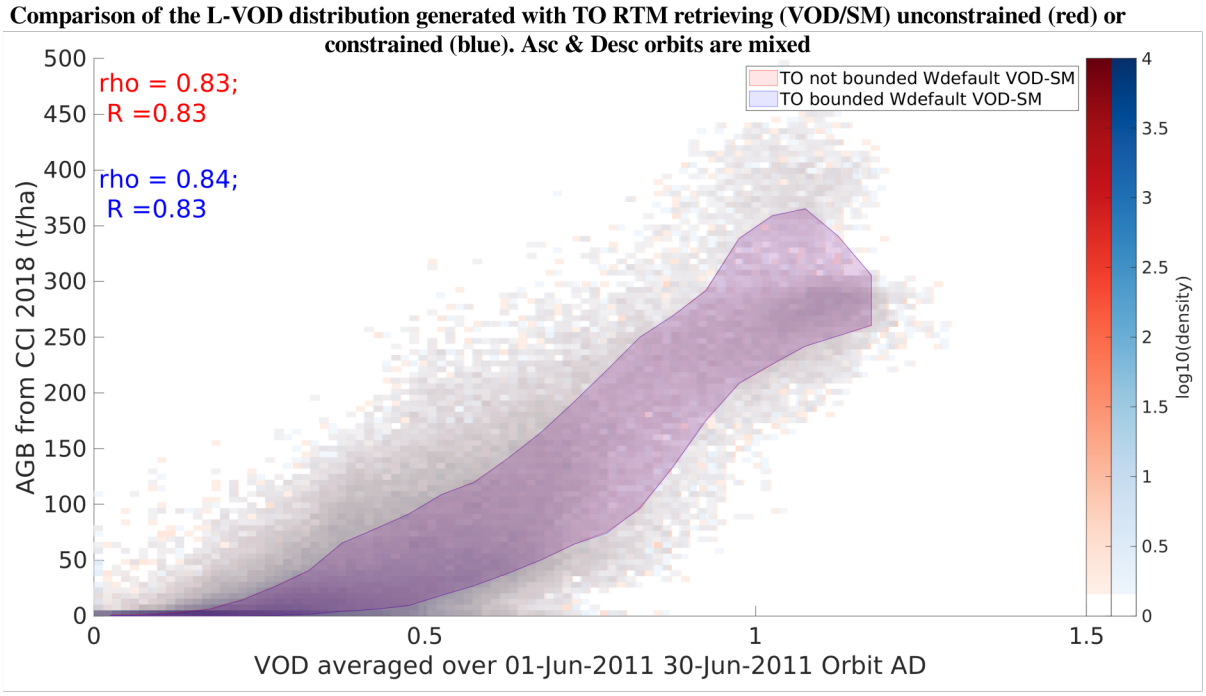

Figure 6: Density plot of the OSMOSE L-VOD for June 2011 against the AGB from CCI 2018. The red color refers to the unconstrained (VOD/SM) retrieval and the blue color to the constrained one. Retrievals were performed with the TO RTM and default values of ω were used. The shaded areas correspond to the interval in-between quantiles 16 and 84 and contain 68% of the distribution.

Fig. 6 shows that constraining the retrieval does not affect the L-VOD correlation to the AGB from CCI 2018. The processing chain is unconstrained for the L-band.

2.3.2 C and X Bands

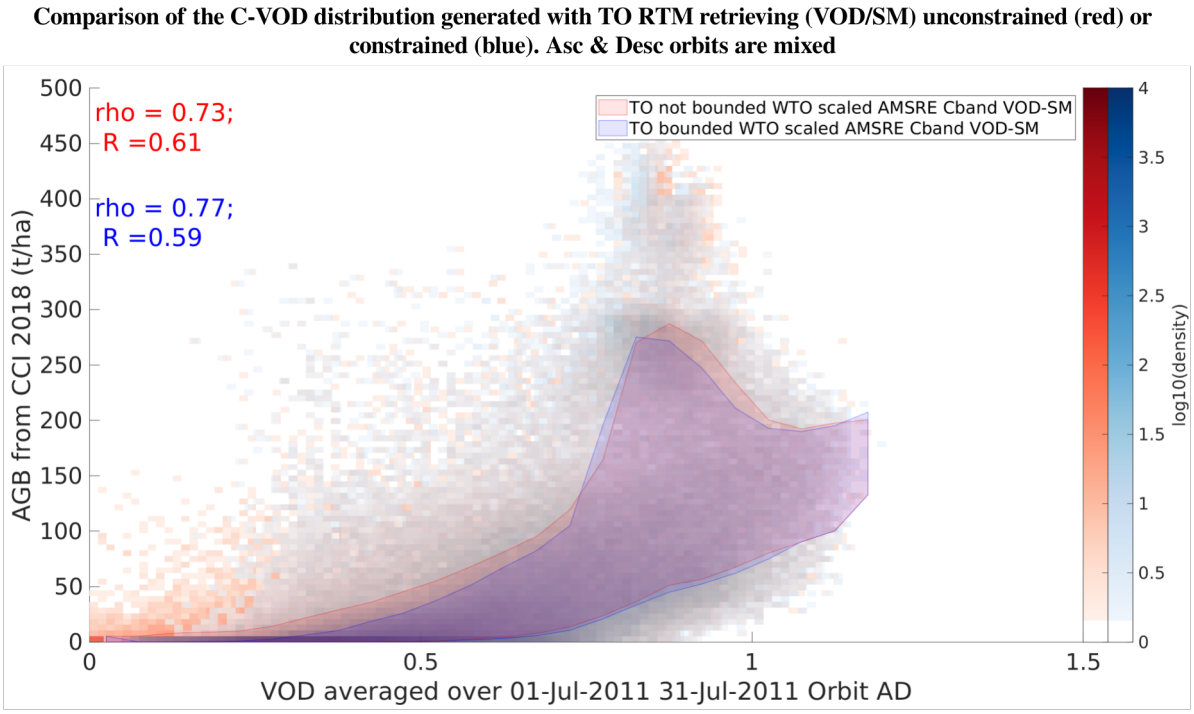

Figure 7: Density plot of the OSMOSE C-VOD for July 2011 against the AGB from CCI 2018. The red color refers to the unconstrained (VOD/SM) retrieval and the blue color to the constrained one. Retrievals were performed with the TO RTM and the values of ω from Fig. 2 were used. The shaded areas correspond to the interval in-between quantiles 16 and 84 and contain 68% of the distribution.

For the C-band, constraining the retrieval slightly improves the VOD Spearman correlation with the AGB (Pearson remains about the same) as displayed on Fig. 7. The dispersion of the C-VOD wrt AGB marginally decreases for VOD values lower than 0.7 when setting lower and upper boundaries to the free parameters. Also, constraining the retrieval greatly improves the convergence between the demo chain (coded in matlab and hosted at CESBIO) and the operational chain (coded in Python and hosted at Magellium). In order to ensure results as close as possible to the demo trials, the retrievals are constrained between [0-2] for the VOD and [0-1] for SM for the C and X bands.

2.4 Influence of the ω and Hr parametrization

Another important aspect of the processing chain is the parametrization of the scattering albedo (ω and the roughness of the soil, Hr). This test was only conducted for the C and X bands as the ω and Hr parametrization for L-band had already been extensively studied and optimized, as described in the literature ((10) and (23)).

For this test, the OSMOSE retrieval platform was run with fixed values for ω and Hr. For the first runs, the ω values spanned [0.01-0.15] and the Hr values spanned [0 0.15 0.3 0.4]. The AMSRE C and X band VOD were derived for the month of July 2011 for ascending and descending orbits. Then, the temporal and spatial mean RMSE between the modeled (TB_{mod}) and the measured TB (TB_{meas}) was computed. This single mean RMSE value allowed us to compare the performance of the different (ω/Hr) configuration. This mean RMSE was either computed over the global region or for continents/regions (Africa, Amazonia, the US) or IGBP vegetation classes (low vegetation or forests). The results of these tests for C-band over the global region are displayed in Fig. 8. This figure shows that Hr has little influence on the RMSE compared to the value of ω. The RMSE slightly decreases from ω=0.01 to ω=0.05. The RMSE then increases with increasing

values of ω. When focusing on particular areas, or particular vegetation classes, the results of this test suggest that an ω value of 0.04 over IGBP low vegetation classes and an ω value of 0.06 over the tropical forests could lead to slightly lower RMSE. This improvement being marginal, the configuration ω=0.05 and Hr=0.15 is selected for the C-band archive. The test was also conducted for the month of September 2011 and led to the same conclusion.

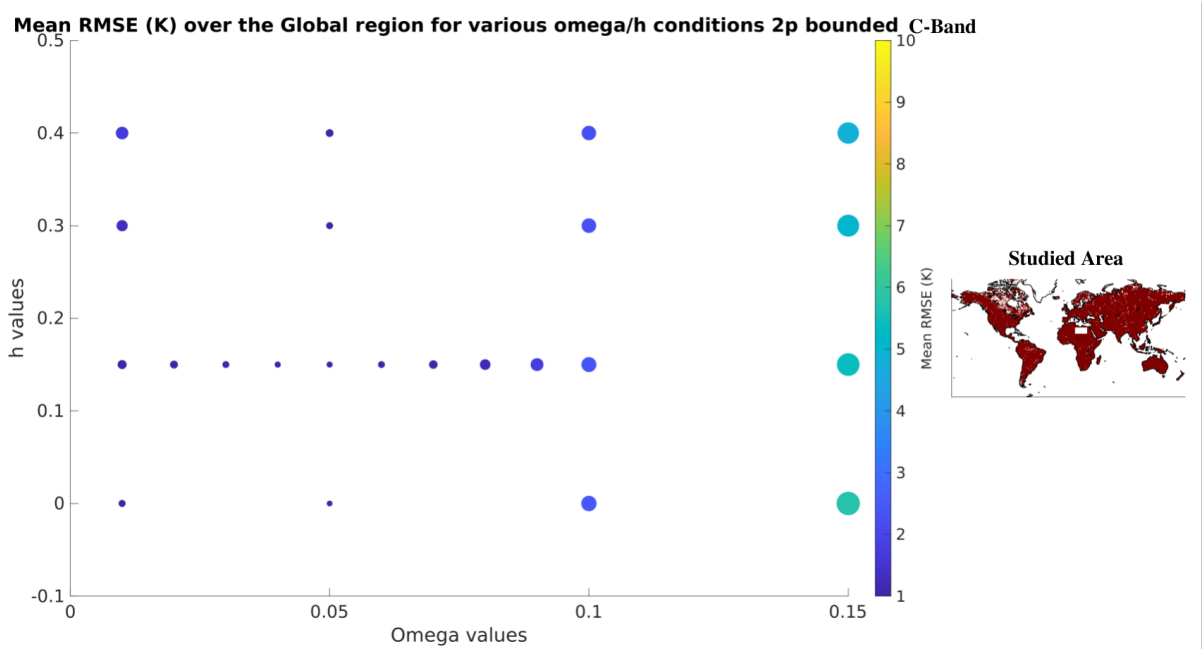

Figure 8: Mean RMSE between C-band $TB_{mod}TB_{meas}$ over the global region for different ω and Hr couples and a 2 parameters (VOD-SM) retrieval. The RMSE was averaged over the course of July 2011, mixing ascending and descending orbits

The same test for the X-band (see Fig. 9) leads to the identical ω and Hr configuration as for the C-band.

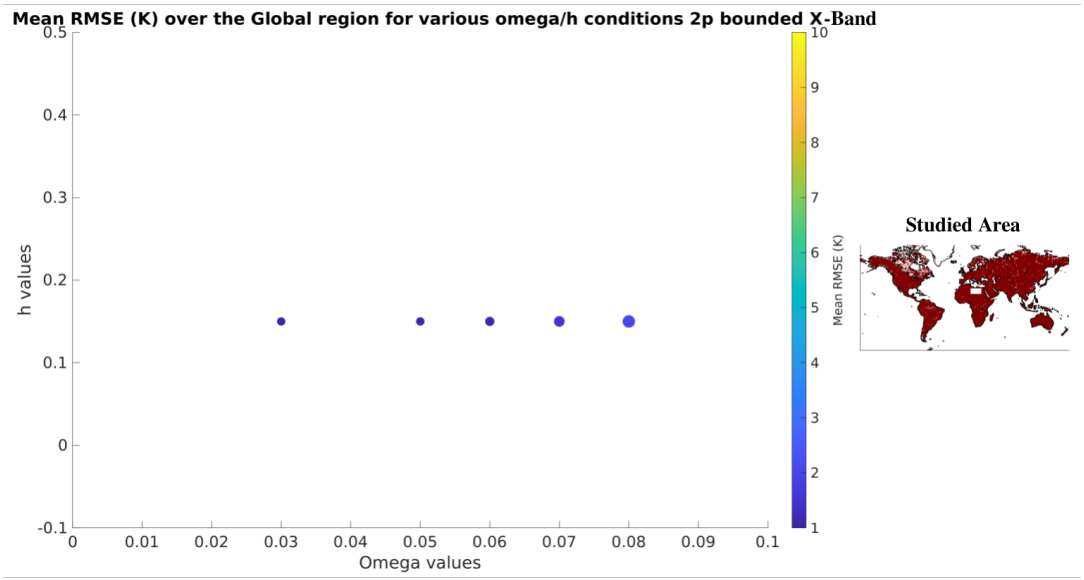

Figure 9: Mean RMSE between X-band $TB_{mod}TB_{meas}$ over the global region for different ω and Hr couples and a 2 parameters (VOD-SM) retrieval. The RMSE was averaged over the course of July 2011, mixing ascending and descending orbits

2.5 Influence of retrieving one or two parameters

As AMSRE and AMSR2 only have one incidence angle, only two TB are available per observation, one for horizontal and one for vertical polarizations. Moreover, these two TB are not completely independent. Retrieving two parameters with two correlated TB may lead to erroneous results. This is why tests with a one-parameter retrieval were conducted with the same configuration as described in the previous section. For various ω and Hr configurations, only the VOD was retrieved, using the SM value from the ERA5 files. The final RMSE was then spatially and temporally (July 2011 ascending and descending orbits) averaged to compare the outputs. The results of these tests for the global region and the C-band are displayed on Fig. 10. When comparing this figure with Fig. 8 from the previous section, it is clear that a one-parameter retrieval leads to higher RMSE between the C-band TB_{mod} and TB_{meas}. The same conclusion applies to the X-band. Hence, a two-parameter retrieval is adopted for the C and X-band archives. As a side note, Fig. 10 is concordant with Fig. 8 and shows the little influence of the value of Hr compared to the value of ω. Again, the lowest global RMSE is achieved with ω=0.05.

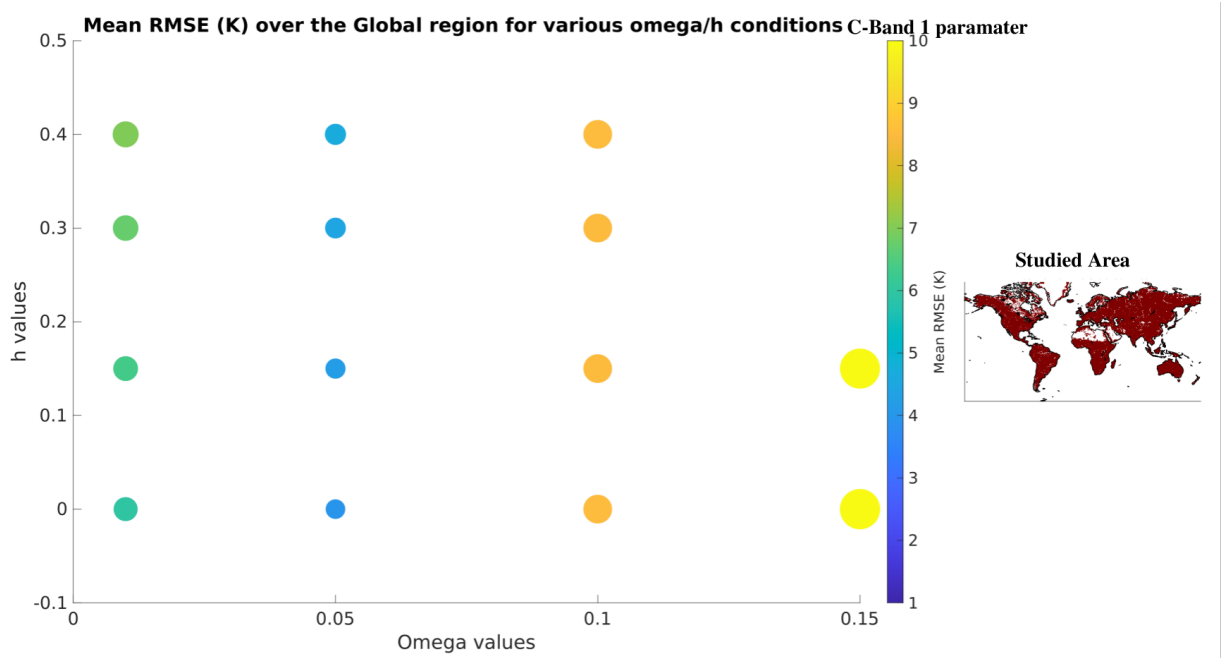

Figure 10: Mean RMSE between C-band $TB_{mod}TB_{meas}$ over the global region for different ω and Hr couples and a 1 parameter (VOD) retrieval. The RMSE was averaged over the course of July 2011, mixing ascending and descending orbits

3 Validation of VOD

3.1 versus datacube2

Datacube 2 is a collection of datasets from visible sensors, projected on the ESA Grid version 2 (5; 6). Refer to documents (7; 9; 8) for a complete description of the datacube2.

3.1.1 L-Band

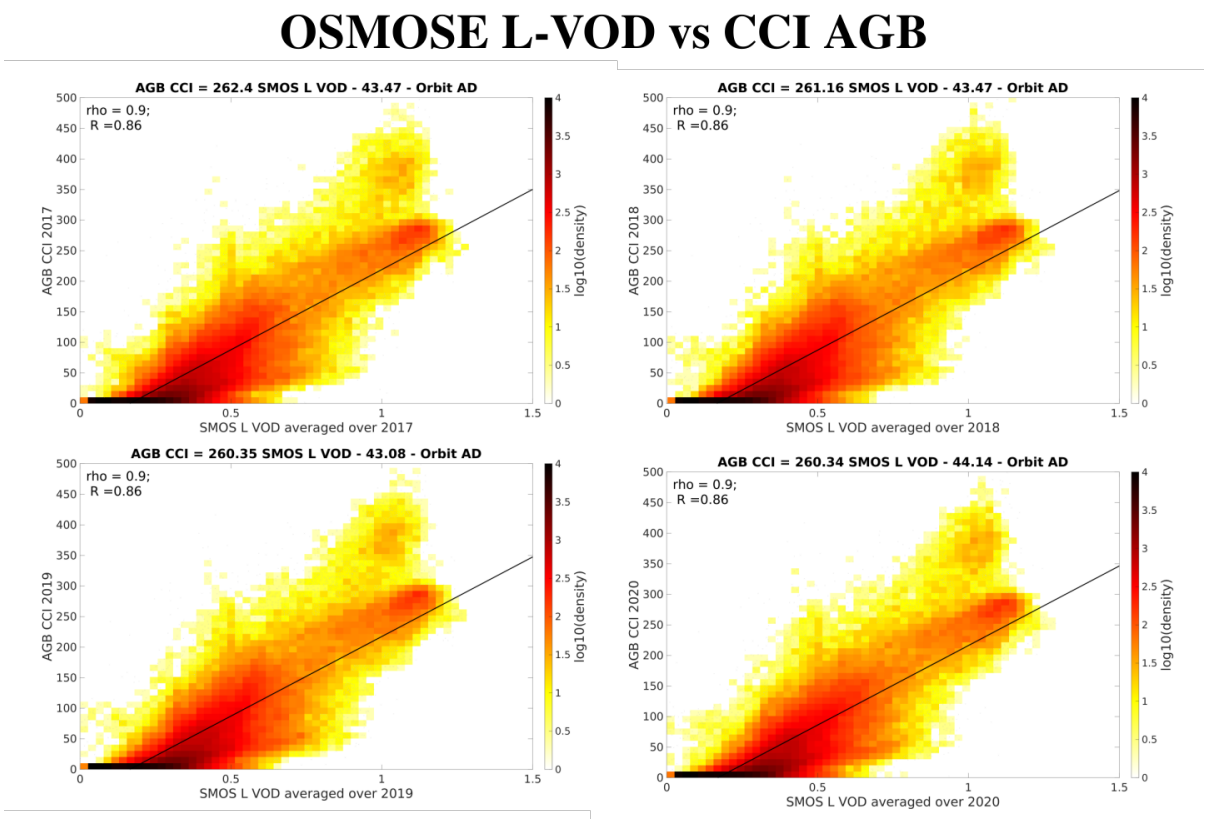

Figure 11: Density plot of the yearly L-VOD from OSMOSE wrt the CCI AGB for the years 2017-2020

Fig. 11 and Table 4 show that the OSMOSE L-VOD is very well correlated to the CCI AGB for all years. The relation is stable from one year to the other.

Table 4: R between the L-VOD from OSMOSE and AGB values from CCI for the years 2017-2020.

	2017	**2018***	**2019**	**2020**
R	0.86	0.86	0.86	0.86
Rho	0.9	0.9	0.9	0.9

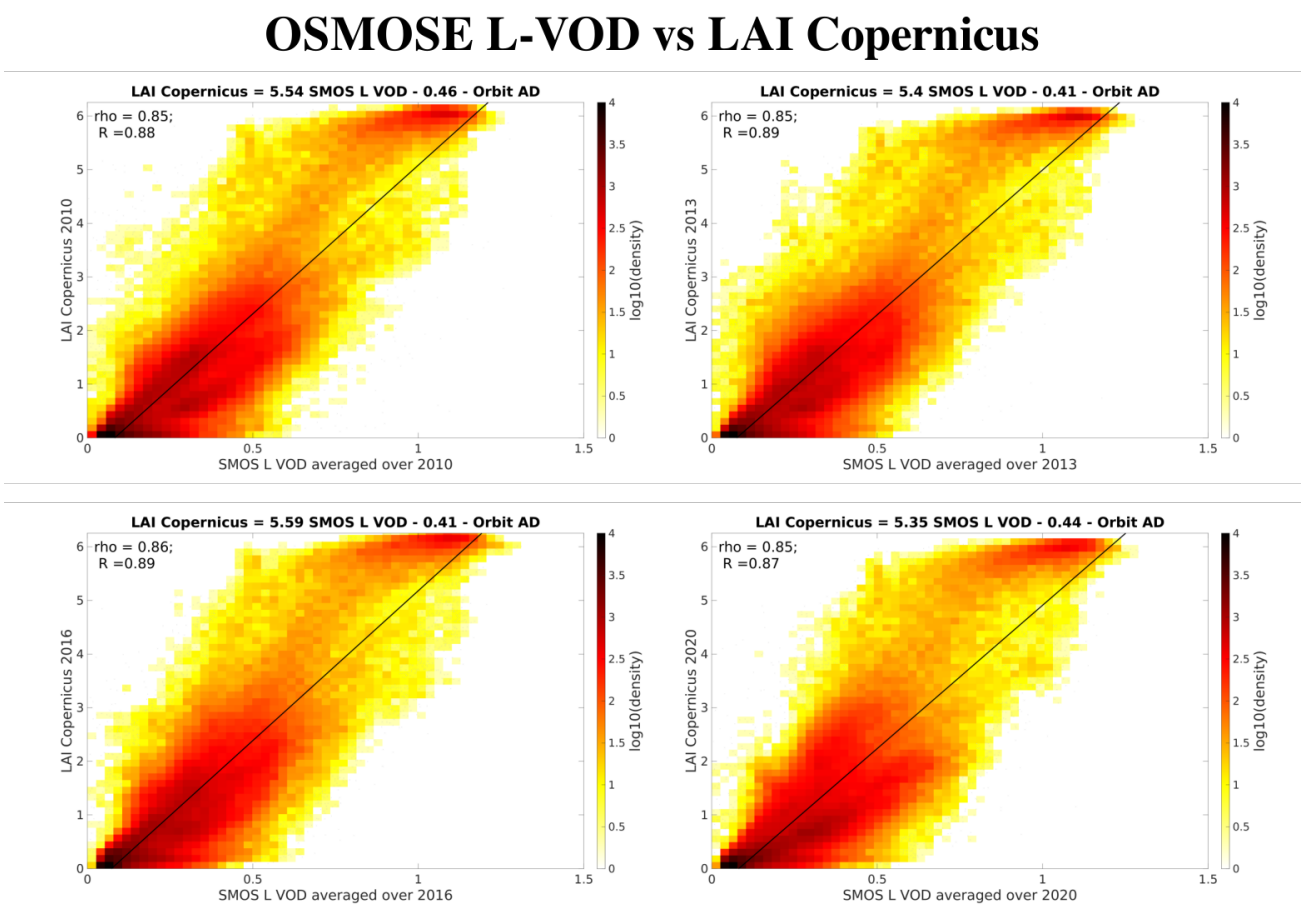

Figure 12: Density plot of the yearly L-VOD from OSMOSE wrt the LAI from Copernicus for the years 2010, 2013, 2016 and 2020

Fig. 12 shows that the OSMOSE L-VOD is very well correlated to the LAI for all years. Only 4 years are displayed on Fig 12, but the relationship is stable from one year to the other.

Even though they are not displayed in this technical note, regressions between the L-VOD and other optical indices have been conducted:

- FAPAR (2010-2016): $0.82 \leq R \leq 0.86$ and $0.82 \leq rho \leq 0.86$
- FCOVER (2010-2020): $0.82 \leq R \leq 0.86$ and $0.81 \leq rho \leq 0.85$
- NDVI (2010-2020): $0.49 \leq R \leq 0.66$ and $0.51 \leq rho \leq 0.7$

3.1.2 C-Band

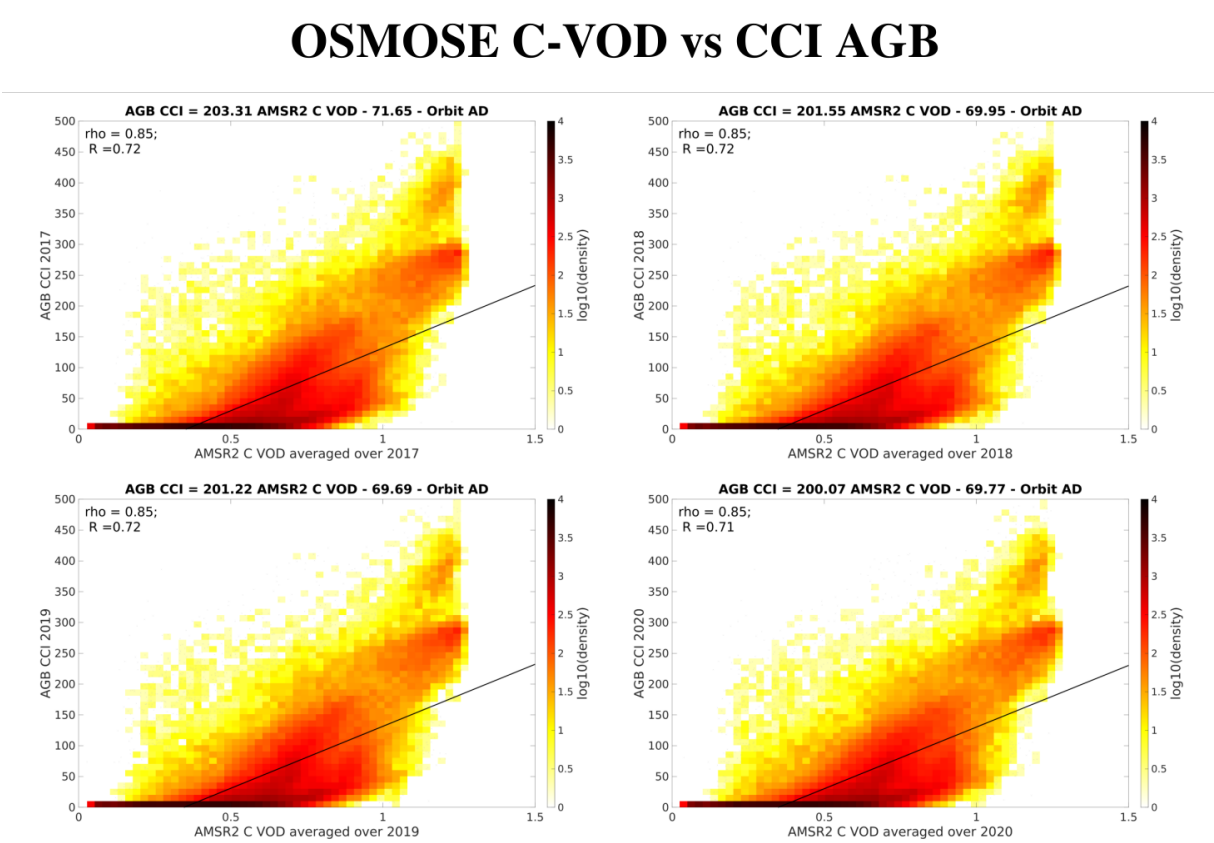

Figure 13: Density plot of the yearly C-VOD from OSMOSE wrt to the AGB from CCI for the years 2017-2020

Fig. 13 shows that the OSMOSE C-VOD is well correlated to the AGB from the CCI for all years and the relation is stable from one year to the other. In agreement with the literature ((15)), the general correlation with the AGB is not as good as with the L-VOD (see Fig. 11).

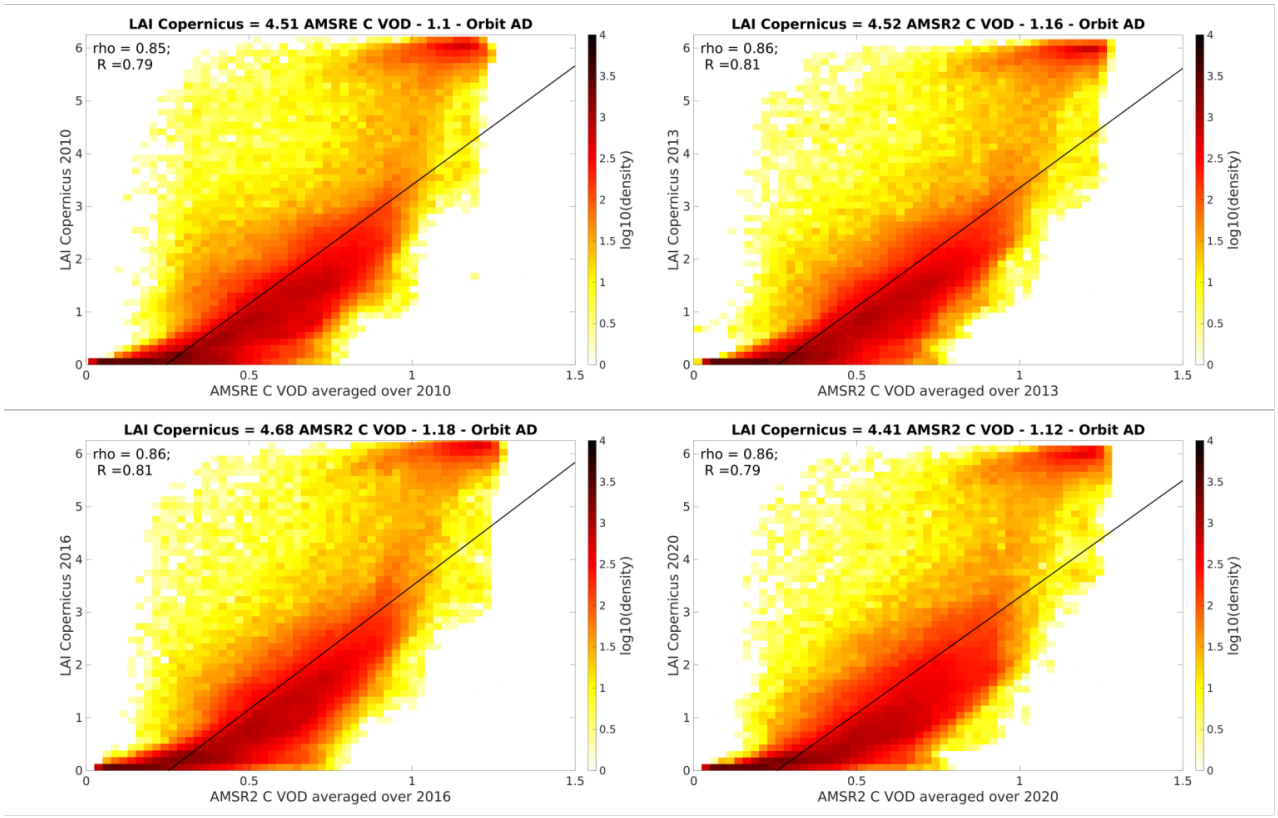

Figure 14: Density plot of the yearly C-VOD from OSMOSE wrt to the LAI from Copernicus for the years 2010, 2013, 2016 and 2020

Fig. 14 shows that the OSMOSE C-VOD is very well correlated to the LAI for all years. Only 4 years are displayed on Fig 14 but the relationship is stable from one year to the other. The linear correlation R is not as good as the one with the LVOD but the spearman correlation coefficients are very close (see Fig. 12).

Even though they are not displayed in this technical note, regressions between the C-VOD and other optical indices have been conducted:

- FAPAR (2002-2016): $0.84 \leq R \leq 0.88$ and $0.84 \leq rho \leq 0.87$
- FCOVER (2002-2020): $0.83 \leq R \leq 0.86$ and $0.83 \leq rho \leq 0.86$
- NDVI (2002-2020): $0.6 \leq R \leq 0.76$ and $0.62 \leq rho \leq 0.77$

3.1.3 X-Band

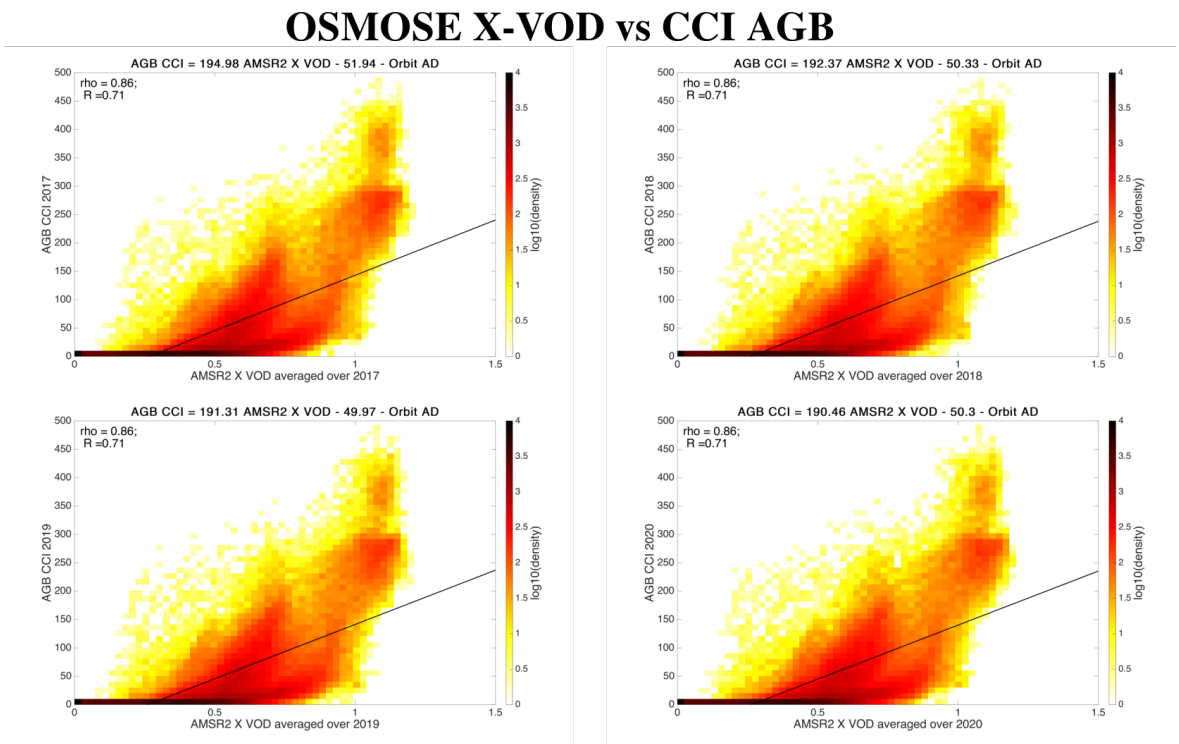

Figure 15: Density plot of the yearly X-VOD from OSMOSE wrt the AGB from CCI for the years 2017-2020

Fig. 15 shows that the OSMOSE X-VOD is well correlated to the AGB from the CCI for all years and the relation is stable from one year to the other. In agreement with the literature ((15)), the general correlation with the AGB is not as good as with the L-VOD (see Fig. 11) but is very close to the correlation of the C-VOD with AGB (see 13).

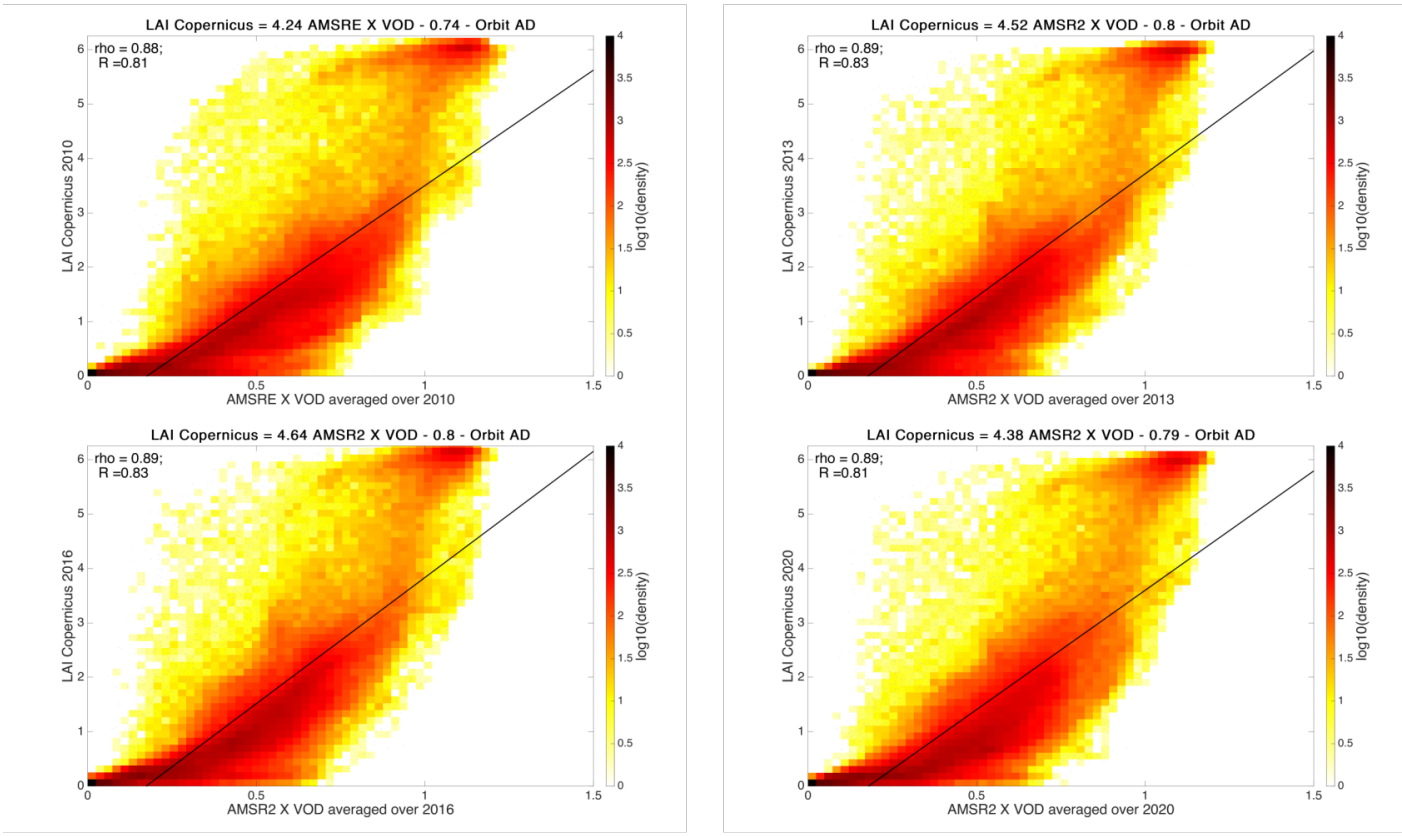

Figure 16: Density plot of the yearly X-VOD from OSMOSE wrt the LAI from Copernicus for the years 2010, 2013, 2016 and 2020

Fig. 16 shows that the OSMOSE X-VOD is very well correlated to the LAI for all years. Only 4 years are displayed on Fig 16 but the relationship is stable from one year to the other. The linear correlation R is not as good as the one with the LVOD but the spearman correlation coefficients are very higher (see Fig. 12). In general, the correlations (R and Rho) are better than the C-VOD ones (see Fig. 14).

Even though they are not displayed in this technical note, regressions between the X-VOD and other optical indices have been conducted:

- FAPAR (2002-2016): $0.86 \leq R \leq 0.90$ and $0.86 \leq rho \leq 0.89$
- FCOVER (2002-2020): $0.87 \leq R \leq 0.89$ and $0.85 \leq rho \leq 0.89$
- NDVI (2002-2020): $0.66 \leq R \leq 0.79$ and $0.68 \leq rho \leq 0.8$

3.2 versus vodca

The version 2 (v2) of the VODCA dataset (25) was just released. In this new version of the dataset, the C, X and Ku bands were merged into one daily data archive. It includes the use of AMSRE and AMSR2 descending orbits processed in the LPRM. The L-band created from SMOS and SMAP ascending orbits processed in the LPRM algorithm, is distributed as a 10-day composite data archive. The full data archive is provided on a 0.25° grid, close to the EASE 2 grid used in the OSMOSE project. The VODCA v2 data archive was reprojected to the OSMOSE grid.

The yearly averaged OSMOSE VOD were compared to the yearly averaged VODCA dataset.

3.2.1 L-band

Fig. 17 shows that the correlation between OSMOSE and VODCA for the L-band is excellent and uniform over the years. The R (Pearson coefficient) and Rho (Spearman coefficient) correlation coefficients are over 0.89 for all years between 2010 and 2020.

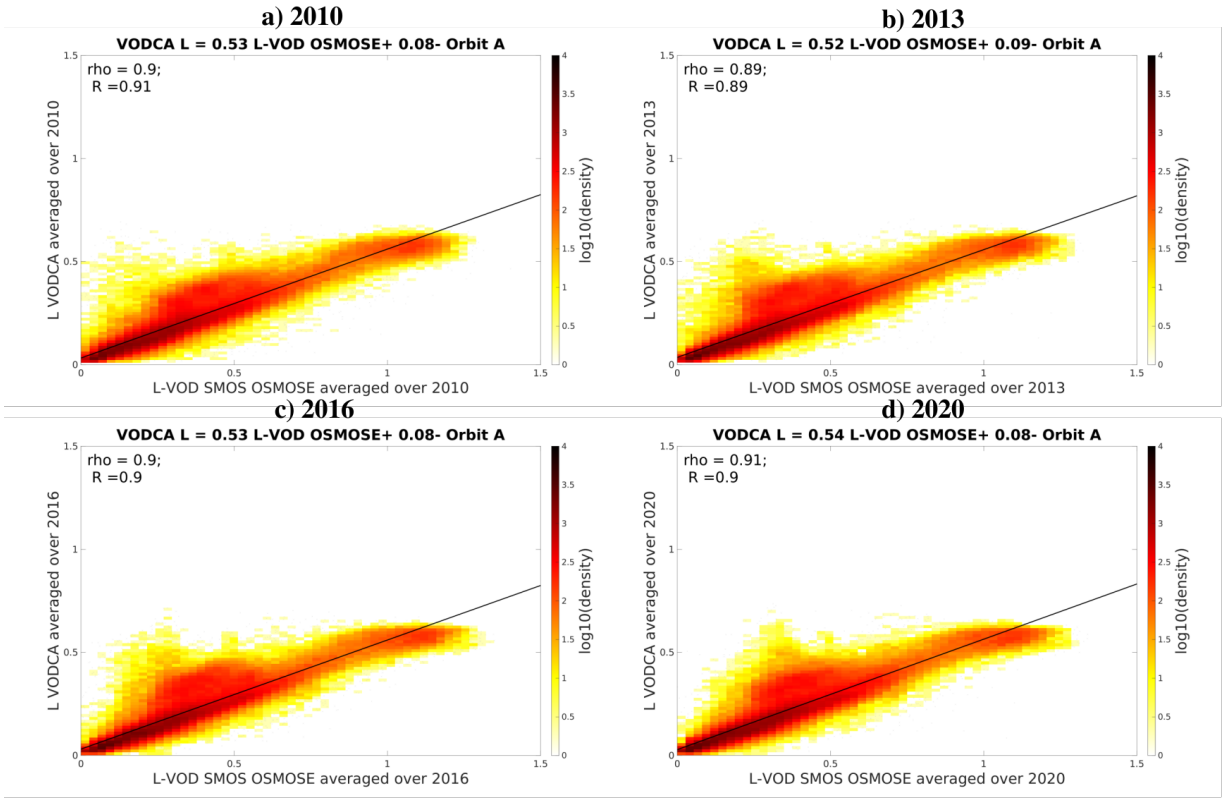

Figure 17: Density plot of the yearly L-VOD from OSMOSE wrt to VODCA v2 for (a) 2010, (b) 2013, (c) 2016 and (d) 2020

Generally, VODCA VOD is lower than OSMOSE VOD, except for a region where the two have more similar values (i.e. 0.2-0.5, above the linear fit black line in Fig. 17). These points are mainly located over boreal forests and further investigation is needed to better understand the difference there. The VODCA VOD also saturates at a lower value (∼0.8) compared to the OSMOSE VOD which saturates at around 1.2 and may be more able to capture the vegetation dynamic.

3.2.2 C -band

Fig. 18 shows that the correlation between OSMOSE and VODCA for the C-band is also excellent and uniform over the years. The ratio between OSMOSE C-band and VODCA CXKu is close to 1. The R and Rho correlation coefficients are over 0.87 for all years between 2003 and 2020.

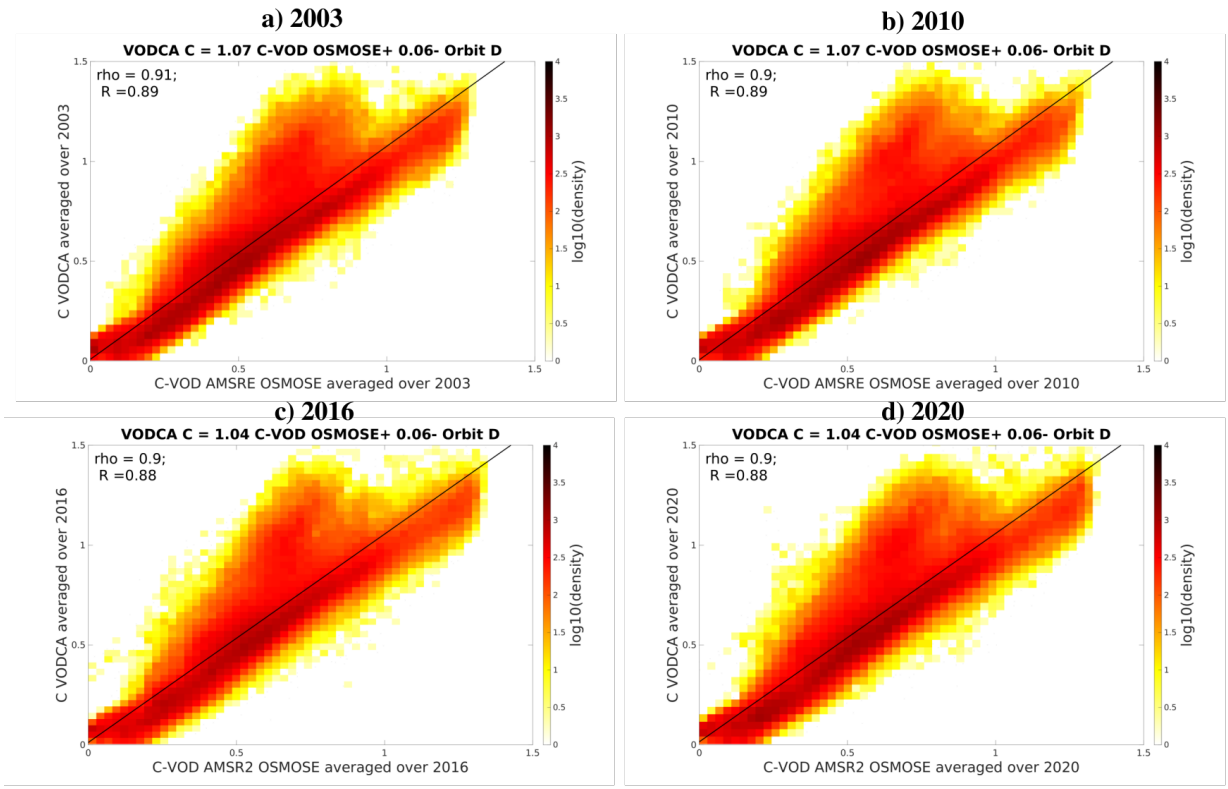

Figure 18: Density plot of the yearly C-VOD from OSMOSE wrt to VODCA CXKu v2 for (a) 2010, (b) 2013, (c) 2016 and (d) 2020

3.2.3 X -band

Fig. 19 shows that the correlation between OSMOSE and VODCA for the X-band is also excellent and uniform over the years. The ratio between OSMOSE X-band and VODCA CXKu is close to 1. The R and Rho correlation coefficients are over 0.88 for all years between 2003 and 2020.

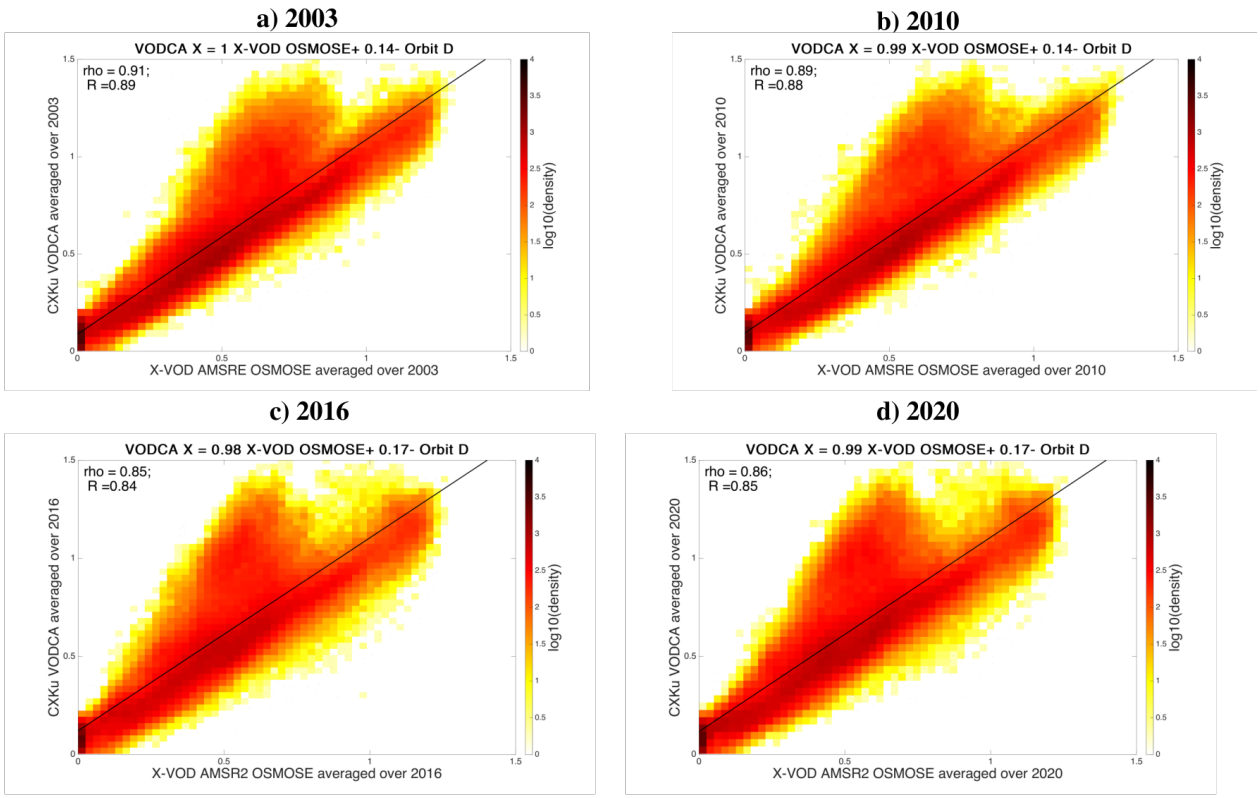

Figure 19: Density plot of the yearly X-VOD from OSMOSE wrt to VODCA CXKu v2 for (a) 2010, (b) 2013, (c) 2016 and (d) 2020

The relationship between OSMOSE C-VOD and VODCA-CXKu (Fig. 18) is very similar to the one between X-VOD and VODCA-CXKu (Fig. 19). The points above the regression line are mainly located in the forests of the northern hemisphere. They are the same across the years and are common to the C and X band as shown on Fig. 20. In these area, the VODCA CXKu VOD are significantly higher than the OSMOSE C and X-VOD.

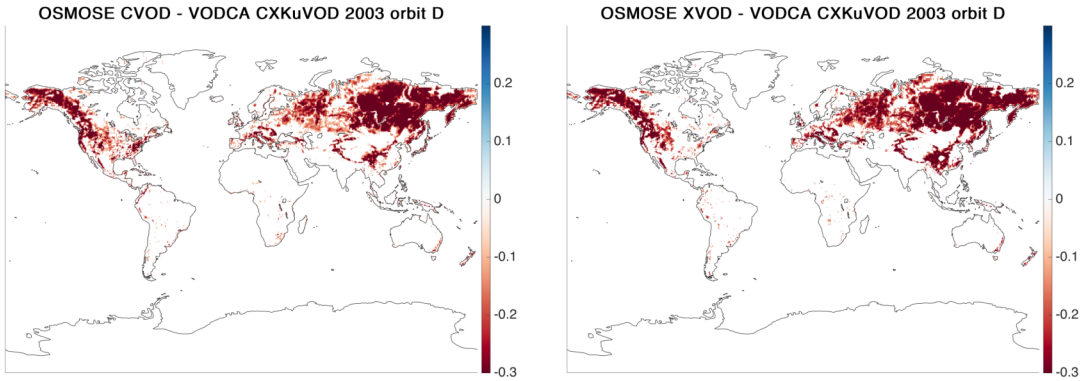

Figure 20: Location of the point above the regression line between OSMOSE and VODCA VOD in 2003 (cf Fig. 18 and 19). Left: C-band and Right: X-band.

3.3 Versus Wang X-VOD

The OSMOSE X-VOD produced with the TO model with ω=0.05 and Hr=0.15 using a constrained 2 parameter retrieval has been compared with the estimation available from (20). In this paper, the authors conduct a regression between the 2017 X-VOD and the AGC from CCI 2017 over Africa. Fig. 21 shows that the OSMOSE X-VOD averaged in 2017 over Africa shows a similar relationship with AGB from CCI as what (20) finds.

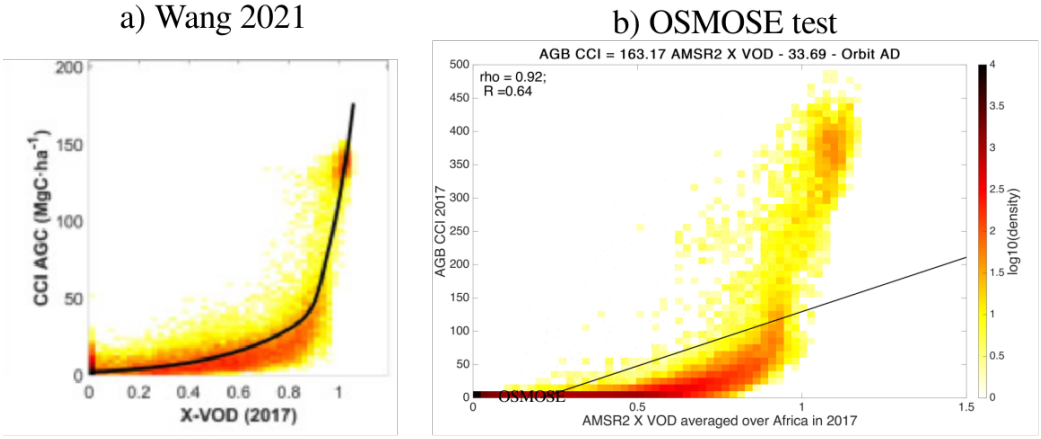

Figure 21: (a) Density plot of the 2017 X-VOD from Fig1 of (20) wrt AGC CCI over Africa. (b) Density plot of the July 2011 OSMOSE X-VOD wrt to AGB CCI over Africa.

3.4 per land classification

A similar evaluation is conducted per land cover classes.

3.4.1 L-band

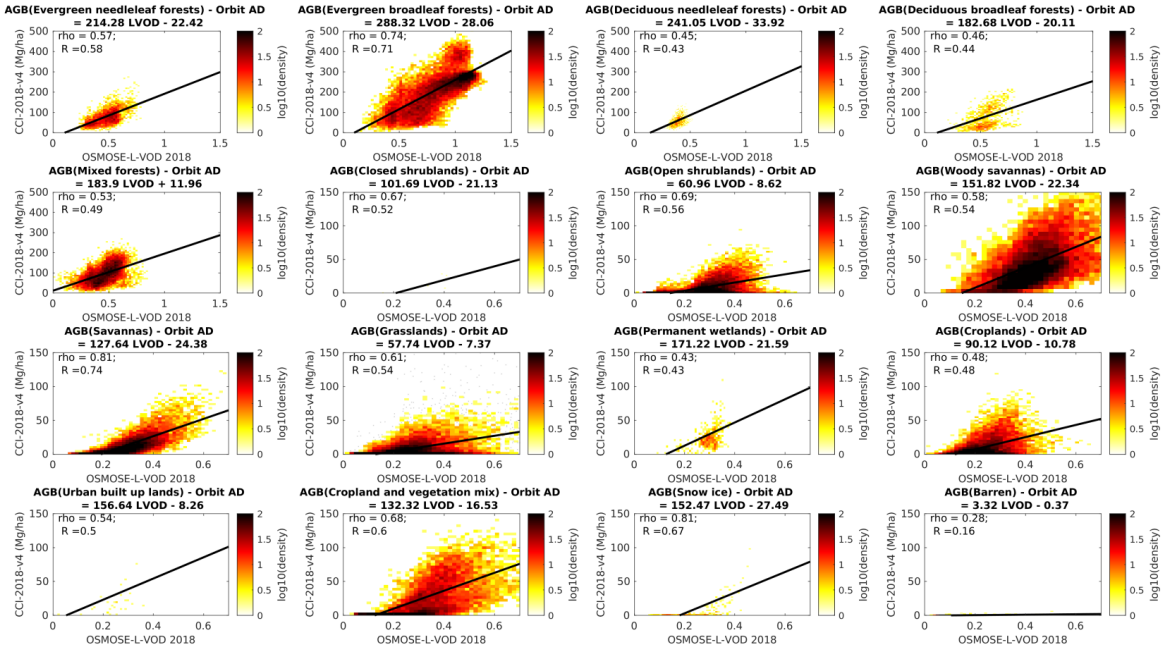

Figure 22: Density plot of the 2018 L-VOD from OSMOSE wrt AGB CCI 2018 per IGBP class

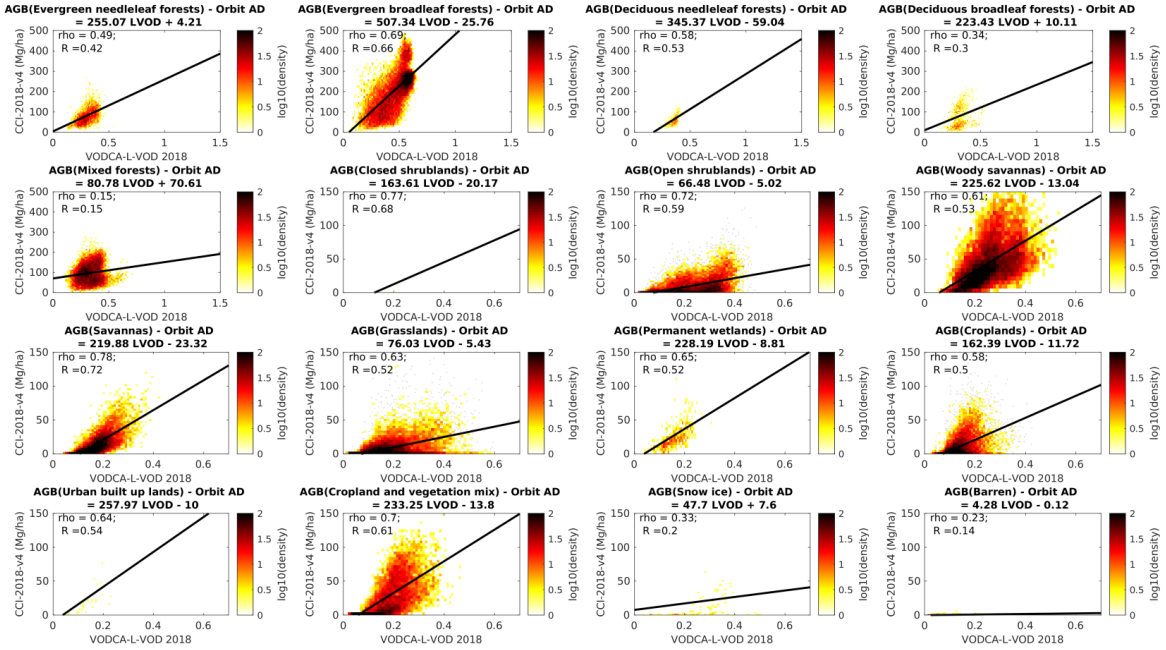

Figure 23: Density plot of the 2018 L-VOD from VODCA v2 wrt CCI 2018 AGB per IGBP classes

Looking at the correlation per IGBP classes, Fig. 22 shows that the correlation is good over Evergreen Broadleaf forests, shrublands, Savannas, grassland and Cropland & Vegetation mix. Interestingly, the correlation is slightly lower over forest classes (except Evergreen Broadleaf forests). The cropland class presents a wide dispersion. Both the CCI-AGB and the VOD are to be considered with care over croplands, the former not being adapted for this type of vegetation, the later varying significantly due to the vegetation water content (i.e. presenting range of values). Over most IGBP classes and all forest classes, OSMOSE L-VOD correlates better with the AGB from CCI 2018 than VODCA L-VOD (see Fig. 23).

3.4.2 C and X bands

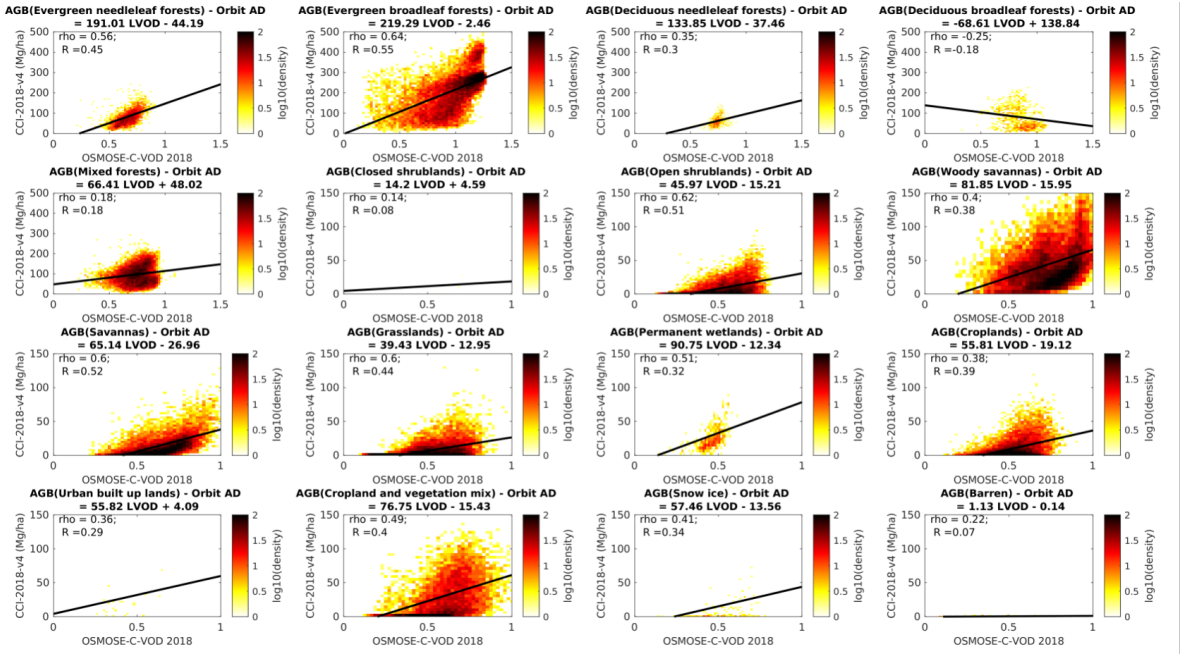

Figure 24: Density plot of the 2018 C-VOD from OSMOSE wrt CCI AGB 2018 per IGBP class

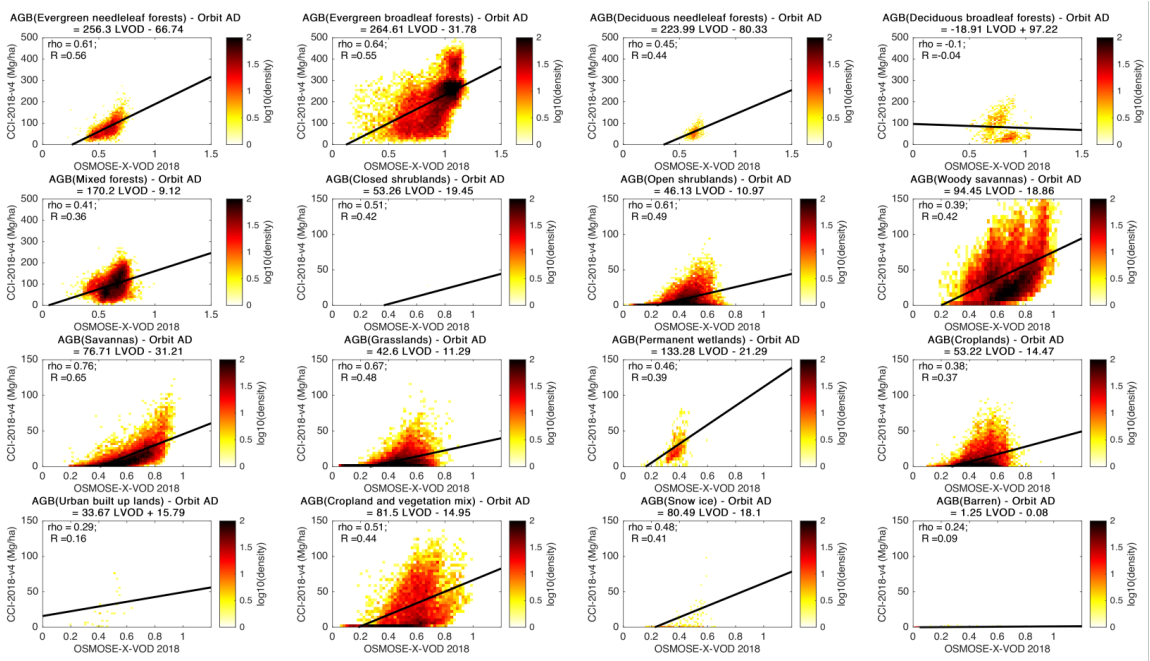

Figure 25: Density plot of the 2018 X-VOD from OSMOSE wrt CCI 2018 AGB per IGBP class

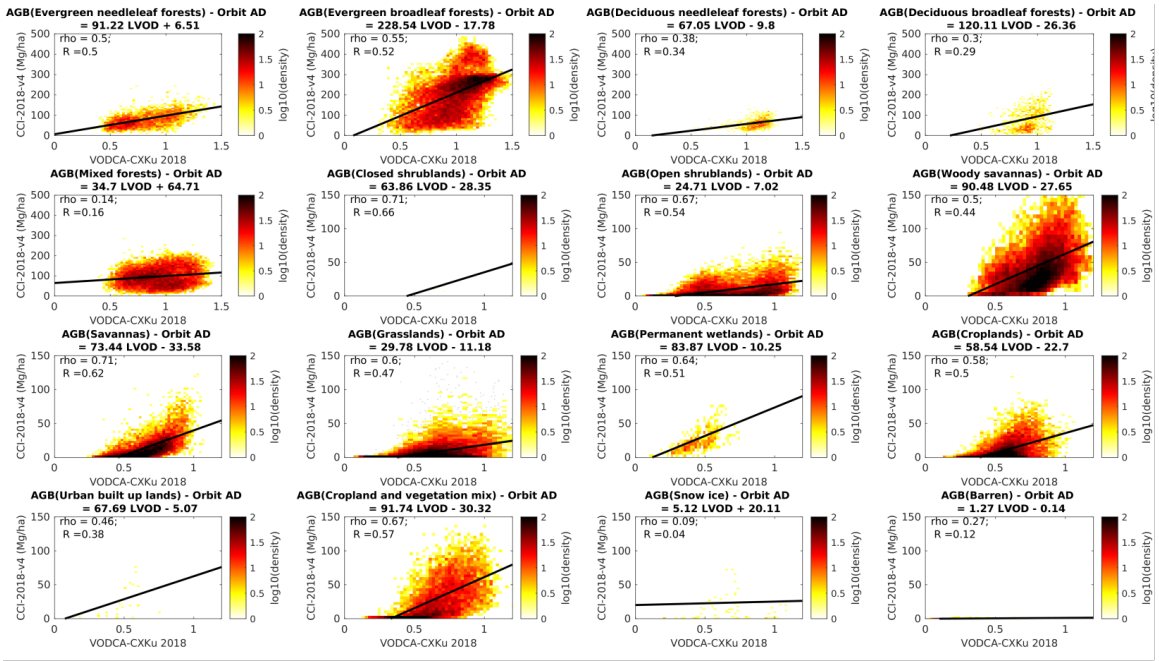

Figure 26: Density plot of the 2018 CXKu-VOD from VODCA v2 wrt CCI 2018 AGB per IGBP class

Looking at the correlation per IGBP classes for the C band, Fig. 24 shows that the correlation is good over Evergreen Broadleaf forests and grassland. In a general way, the correlation is not excellent. For most vegetation classes, the OSMOSE C-VOD has similar correlation with the AGB as the VODCA CXKU (see Fig. 26), though the AGB correlation with OSMOSE C-VOD is slightly lower. The X-band (Fig. 25) shows a good correlation over Savannas. For other vegetation classes, the correlations lay below 0.6. The X-band has similar correlation coefficient per IGBP class as the C-band and the VODCA-CXKu dataset.

Table 5 gathers all the correlation coefficients per IGBP class for OSMOSE L and C VOD and VODCA L and CXKu VOD.

Table 5: Correlation Coefficient (R) between the CCI AGB (year 2018) and VODs from OSMOSE (L/C/X) and VODCA.

	OSMOSE L-VOD	VODCA L-VOD	OSMOSE C-VOD	OSMOSE X-VOD	VODCA CXKU-VOD
Evergreen needleleaf forests	**0.58**	0.42	0.45	0.56	0.50
Evergreen broadleaf forests	**0.71**	0.66	0.55	0.55	0.52
Deciduous needleleaf forests	0.43	**0.53**	0.3	0.44	0.34
Deciduous broadleaf forests	**0.44**	0.3	-0.18	-0.04	0.29
Mixed forests	**0.49**	0.15	0.18	0.36	0.16
Closed shrublands	0.52	**0.68**	0.08	0.42	0.66
Open shrublands	0.56	**0.59**	0.51	0.49	0.54
Woody savannas	**0.54**	0.53	0.38	0.42	0.44
Savannas	**0.74**	0.72	0.52	0.65	0.62
Grasslands	**0.54**	0.52	0.44	0.48	0.47
Permanent wetlands	0.43	**0.52**	0.32	0.39	0.51
Croplands	0.48	**0.50**	0.39	0.37	0.50
Urban	0.50	**0.54**	0.29	0.16	0.38
Cropland and vegetation mix	0.60	**0.61**	0.4	0.44	0.57
Snow Ice	**0.67**	0.20	0.34	0.41	0.04
Barren	**0.16**	0.14	0.07	0.09	0.12

4 AMSRE/AMSR2

AMSR2 is the follow-up mission of AMSRE and there is a nine-month gap between both sensors. One of the objectives of the OSMOSE project being to build a 20-year time series of C and X VOD, the continuity of the AMSRE/AMSR2 data needs to be assessed and potentially corrected. Several studies have already dealt with AMSRE/2 continuity and put up different methodologies. (22) established a linear relationship between the AMSRE and AMSR2 TB (in H and V polarization respectively) over stable and homogeneous land covers (Evergreen Broadleaf forest and snow and ice). This relationship was then applied globally to calibrate the AMSRE TB to the AMSR2 ones. Finally, the calibrated TB were in turn processed by the X-MEB ((21)) to produce a consistent 20-year long X-VOD time series. The authors of (14) and (25) worked directly on the VOD and employed CDF matching techniques to scale AMSR2 to AMSRE. The following sentences are directly extracted from (25): *VODCA v1 scaled AMSR2 to TMI if enough overlap was available or directly to AMSR-E, without temporal overlap, above and below 35° latitude N and S, respectively (14). This led to spatial inconsistencies in VODCA v1 [...]. Therefore, we changed the approach in VODCA v2 and used SSMI F17 Ku-band observations (scaled to AMSR-E X-band) as reference to bridge the gap between AMSR-E and AMSR.*

For the OSMOSE project, the bias and scaling are studied and performed directly on the C and X-VOD of AMSRE and AMSR2 and the datacube #2 is used to check the consistency of the correction.

4.1 Assessment of the AMSRE/AMSR2 bias for the C-band

Since there is no overlap between AMSRE and AMSR2, the continuity of the VOD between both sensors was studied by taking into account the last year and a half of AMSRE (1st Jan 2010 to 27th Sep 2011) and the first year and a half of AMSR2 (3rd Jul. 2012 to 31st Dec. 2014), following the method described in (14). The mean of the C-VOD was computed for both sensors over their respective time period. The difference between the mean VOD is then computed. This difference is referred to as bias even though it does not purely represent a bias as there is no overlap between the sensors.

To better understand the bias between AMSRE and AMSR2 C-VOD, it is compared to the mean difference of various optical indices from the datacube #2 (FAPAR, FCOVER, LAI, NDVI) and also to the mean difference of the OSMOSE L-VOD over the same time period. The global spatial correlation between the C-VOD bias and the optical indexes/L-VOD is also computed. The results appear in Fig. 27 to 31.

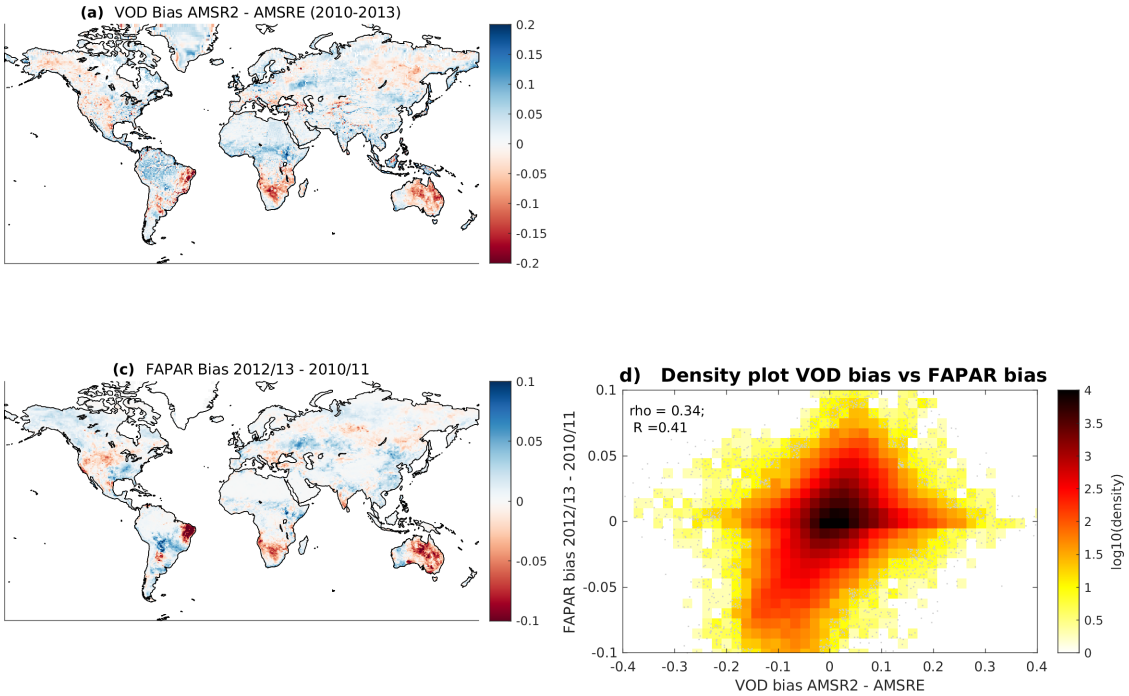

Figure 27: (a) Mean difference between the AMSRE C-VOD (01/01/2010-09/27/2011) and the AMSR2 C-VOD (07/03/2012-12/31/2013). (c) Mean difference of the FAPAR between 2012/2013 and 2010/2011. (d) Global spatial correlation between FAPAR and C-VOD bias.

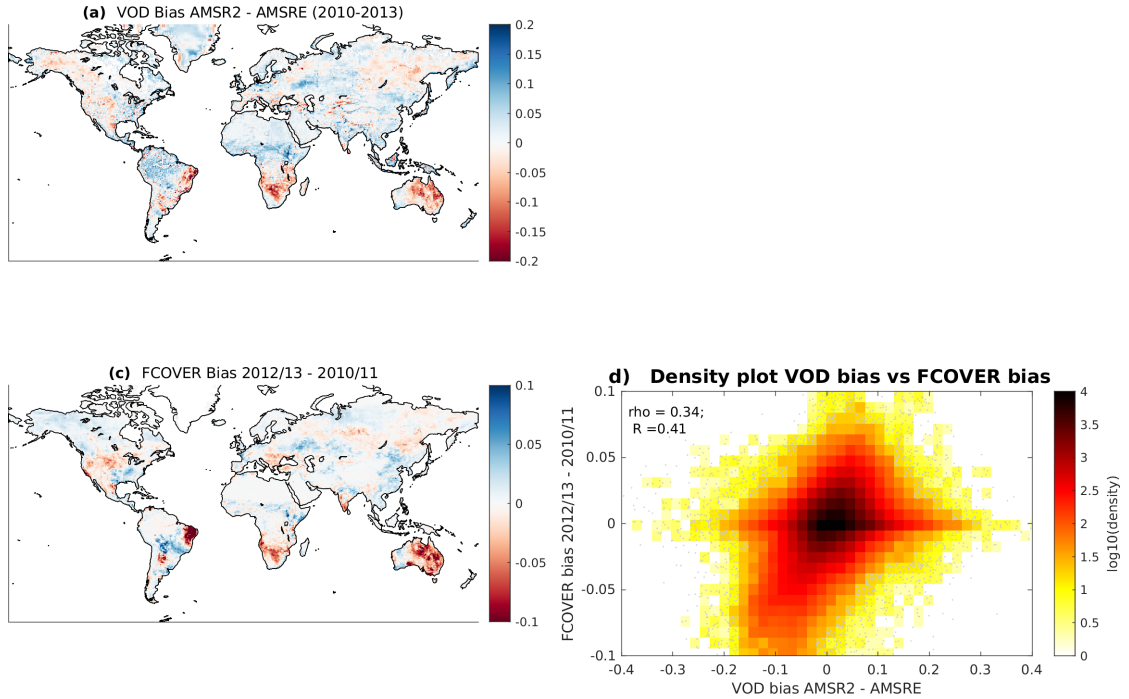

Figure 28: (a) Mean difference between the AMSRE C-VOD (01/01/2010-09/27/2011) and the AMSR2 C-VOD (07/03/2012-12/31/2013). (c) Mean difference of the FCOVER between 2012/2013 and 2010/2011. (d) Global spatial correlation between FCOVER and C-VOD bias.

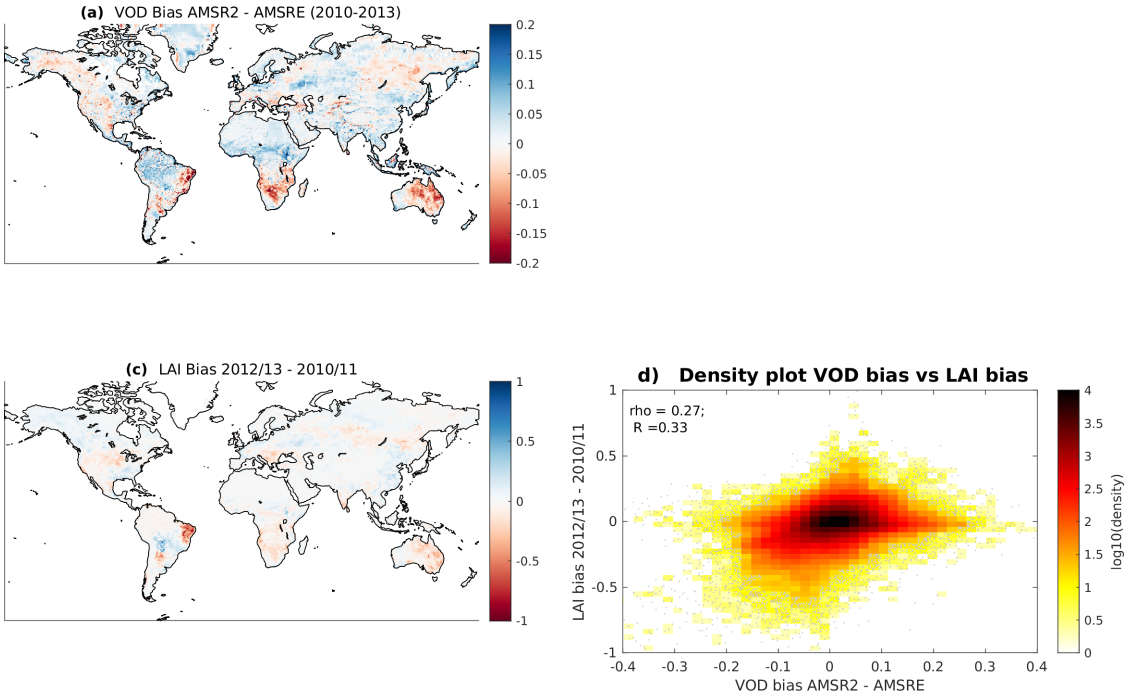

Figure 29: (a) Mean difference between the AMSRE C-VOD (01/01/2010-09/27/2011) and the AMSR2 C-VOD (07/03/2012-12/31/2013). (c) Mean difference of the LAI between 2012/2013 and 2010/2011. (d) Global spatial correlation between LAI and C-VOD bias.

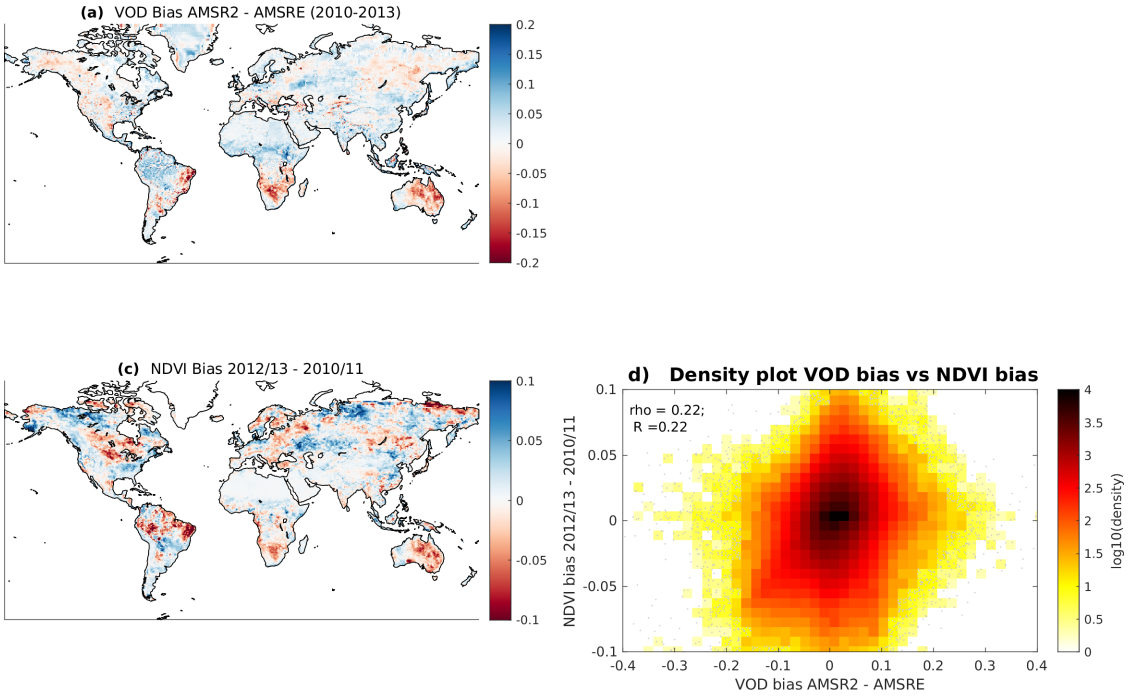

Figure 30: (a) Mean difference between the AMSRE C-VOD (01/01/2010-09/27/2011) and the AMSR2 C-VOD (07/03/2012-12/31/2013). (c) Mean difference of the NDVI between 2012/2013 and 2010/2011. (d) Global spatial correlation between NDVI and C-VOD bias.

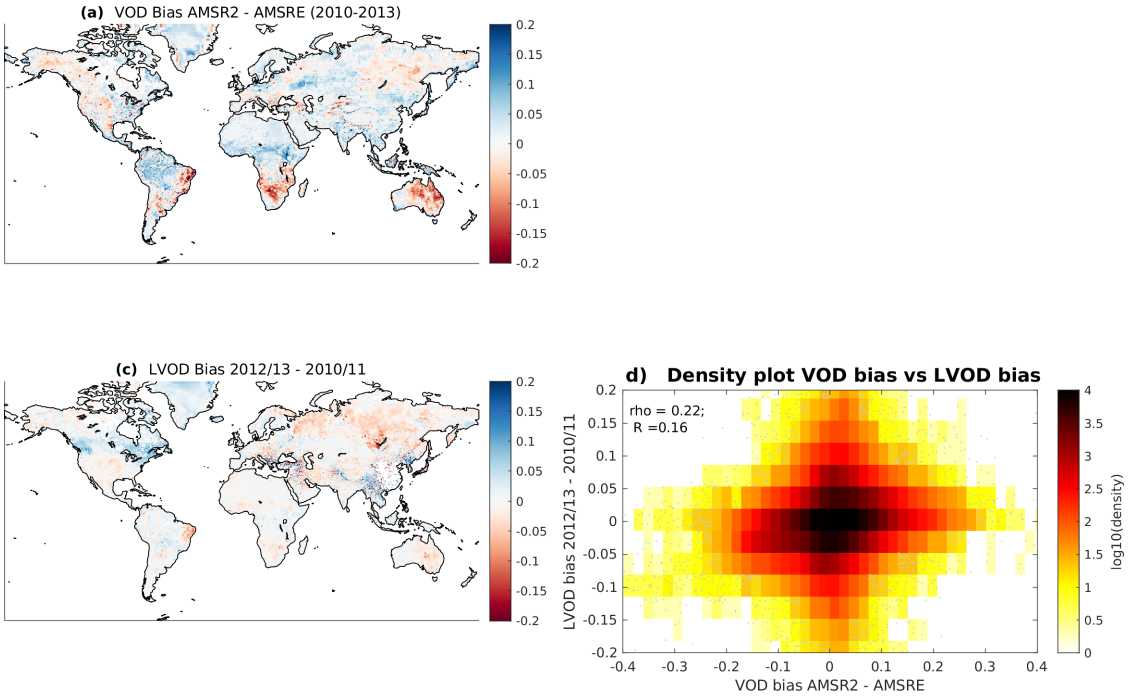

Figure 31: (a) Mean difference between the AMSRE C-VOD (01/01/2010-09/27/2011) and the AMSR2 C-VOD (07/03/2012-12/31/2013). (c) Mean difference of the L-VOD between 2012/2013 and 2010/2011. (d) Global spatial correlation between L-VOD and C-VOD bias.

Globally, the C-VOD bias is not correlated to any of the optical indices or L-VOD bias. R is lower than 0.41 for all cases and Rho is lower than 0.34. This indicates that globally, the C-VOD bias is not natural. Interestingly, Fig. 31 shows that the C-VOD bias is much more dynamic than the L-VOD bias. However, looking up Fig. 27 to Fig. 31, 3 areas have similar C-VOD biases and optical/L-VOD biases: the eastern tip of Brazil, northern South Africa, and eastern Australia. For these 3 regions the observed C-VOD bias is also observed in the optical indices/L-VOD bias as well, meaning that the C-VOD bias there is (at least) partly natural.

4.2 Correction of the AMSRE/AMSR2 bias

These comparisons highlight that globally the bias between AMSRE and AMSR2 needs to be corrected pixel wise. One well established method to correct a bias is the Cumulatice Distribution Function (CDF) matching as described and applied in section III.B. of (13). The following sentences are directly extracted from (13): *The CDF is a specific way to describe the distribution of a discrete or continuous variable X. The purpose of this function is to give the probability that X will take a value less than or equal to a certain threshold. [...] CDF matching consists of transforming the CDF of one variable X (source data) to mimic that of another variable Y (reference data) by using a function f.*

For this study, AMSRE is rescaled to AMSR2 as AMSR2 is the most recent sensor. As a consequence, the source data are the last two years of AMSRE (28th Sept. 2009 to 27th Sept. 2011) and the reference data are the first two years of AMSR2 (3rd Jul. 2012 to 2nd Jul 2014). Different CDF matching functions can be used. The most simple one is a linear function using the mean and the standard deviation of the source and reference data. To use the linear CDF matching, the data time series need to be Gaussian. Several statistical tests (Chi-square goodness-of-fit test, the Lilliefors test (12) and the Jarque-Bera test (11)) were applied on the AMSRE and AMSR2 C-VOD time series. These stastistical tests showed that the 2-year long time series could not be considered as Gaussian. Hence, the Polynomial fitting CDF matching from (4) was used to rescale AMSRE to AMSR2. (13) summarizes the principle: It *uses a function approximation technique to find the relationships between the source and the reference data CDF. First, the source and reference CDFs are computed with the number of percentiles equal to the number of SM observations in their respective time series. Second, the source CDF is linearly interpolated on the percentiles of the reference CDF, and*

the difference between the two is computed. Then, the difference is plotted against the interpolated source CDF, and a polynomial fit is performed. Finally, the polynomial function is used to compute the correction to apply to the source data. As mentioned in (1), this method has the advantage to provide a continuous transformation, but it is more complex to control. Indeed, it can be subjected to instabilities, and extreme events are not sure to be well preserved.

A polynomial of degree three was used to rescale the C-VOD time series of each pixel. If there are fewer than 50 points in either the source or reference time series, the pixel is dropped (4 points in total).

4.3 Validation of the CDF matching

Time series of VOD with/without CDF matching correction are checked against SMOS L-VOD and optical indices from OSMOSE data cube 2. The figures focus particularly on the three areas highlighted in section 4.1.

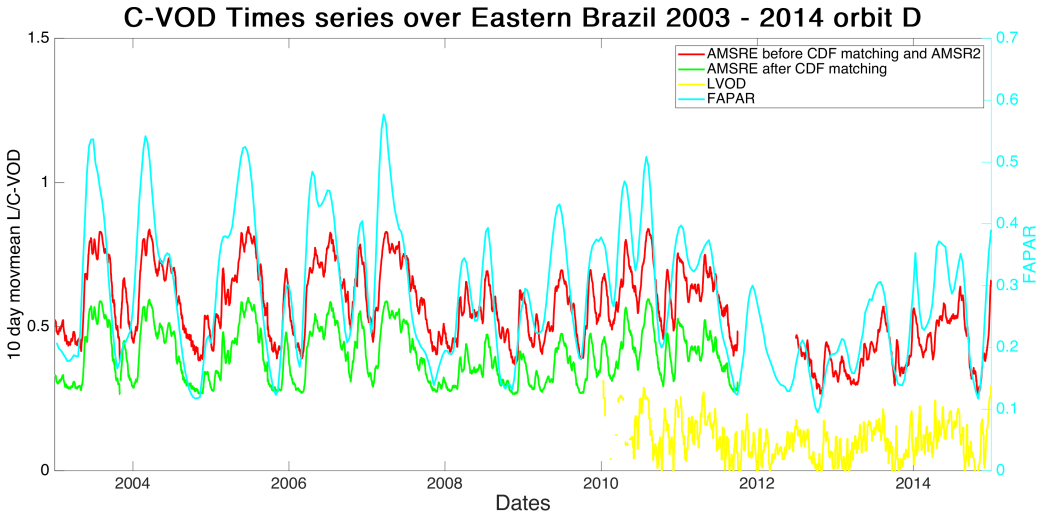

Figure 32: For the point [-11.41° N, -39.77°E] (eastern tip of Brazil): 2003-2014 time series of the AMSRE/AMSR2 C-VOD before CDF matching (red), 2003-2011 time series of AMSRE C-VOD after CDF matching with AMSR2 (green), 2010-2014 time series of the SMOS L-VOD (yellow), 2003-2014 time series of FAPAR from Copernicus (cyan). The L/C-VOD time series are 10 day moving averages.

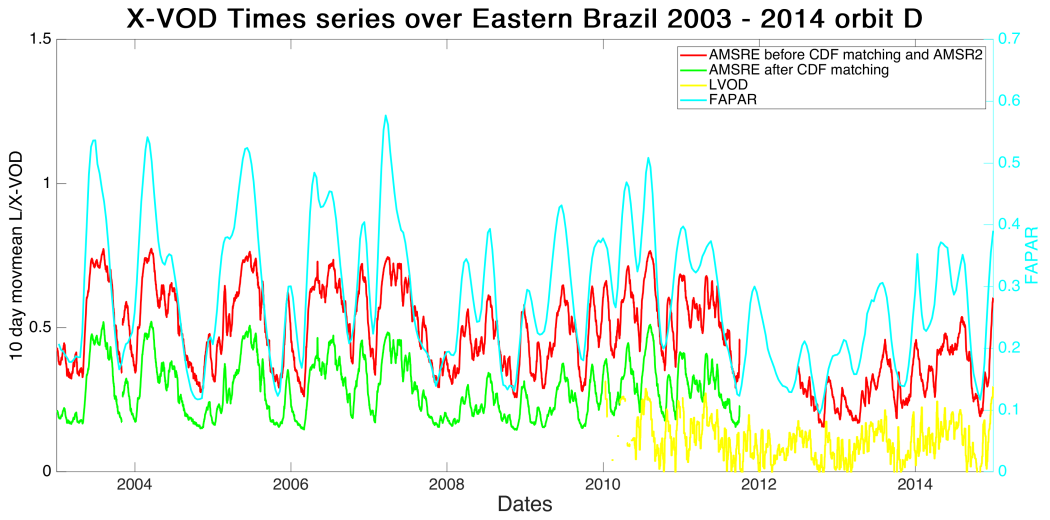

Figure 33: For the point [-11.41° N, -39.77°E] (eastern tip of Brazil): 2003-2014 time series of the AMSRE/AMSR2 X-VOD before CDF matching (red), 2003-2011 time series of AMSRE X-VOD after CDF matching with AMSR2 (green), 2010-2014 time series of the SMOS L-VOD (yellow), 2003-2014 time series of FAPAR from Copernicus (cyan). The L/C-VOD time series are 10 day moving averages.

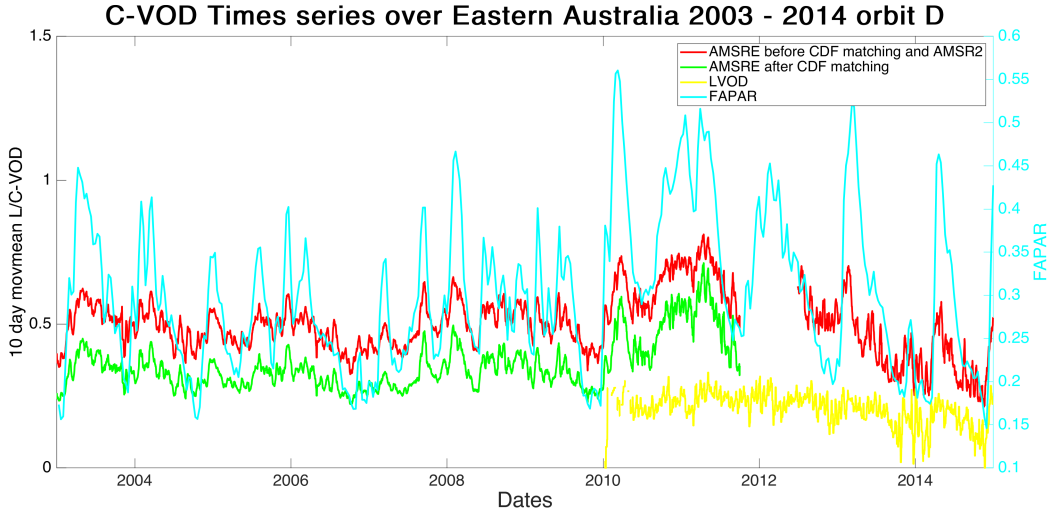

Figure 34: Time series for the point [-26.3° N, 149.8°E] (eastern Australia): 2003-2014 of the AMSRE/AMSR2 C-VOD before CDF matching (red), 2003-2011 time series of AMSRE C-VOD after CDF matching with AMSR2 (green), 2010-2014 time series of the SMOS L-VOD (yellow), 2003-2014 time series of FAPAR from Copernicus (cyan). The L/C-VOD time series are 10 day moving averages.

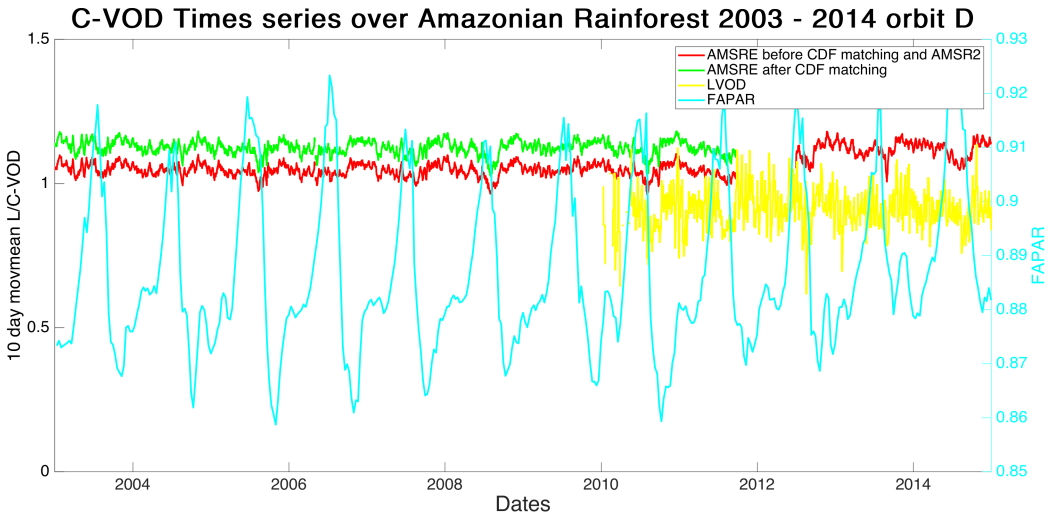

Figure 35: For the point [-7.4° N, -60.6°E] (Amazonian rain-forest): 2003-2014 time series of the AMSRE/AMSR2 C-VOD before CDF matching (red), 2003-2011 time series of AMSRE C-VOD after CDF matching with AMSR2 (green), 2010-2014 time series of the SMOS L-VOD (yellow), 2003-2014 time series of FAPAR from Copernicus (cyan). The L/C-VOD time series are 10 day moving averages.

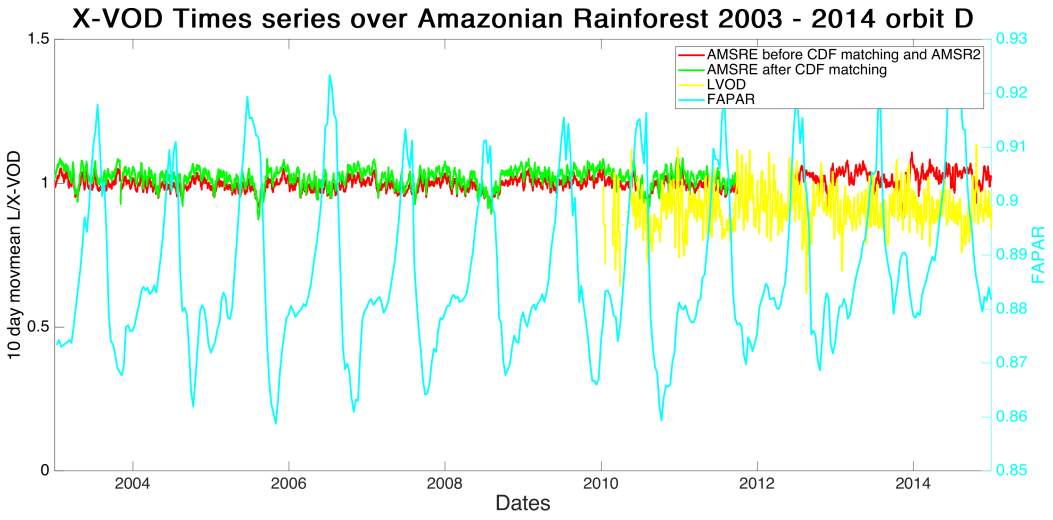

Figure 36: For the point [-7.4° N, -60.6°E] (Amazonian rain-forest): 2003-2014 time series of the AMSRE/AMSR2 X-VOD before CDF matching (red), 2003-2011 time series of AMSRE X-VOD after CDF matching with AMSR2 (green), 2010-2014 time series of the SMOS L-VOD (yellow), 2003-2014 time series of FAPAR from Copernicus (cyan). The L/C-VOD time series are 10 day moving averages.

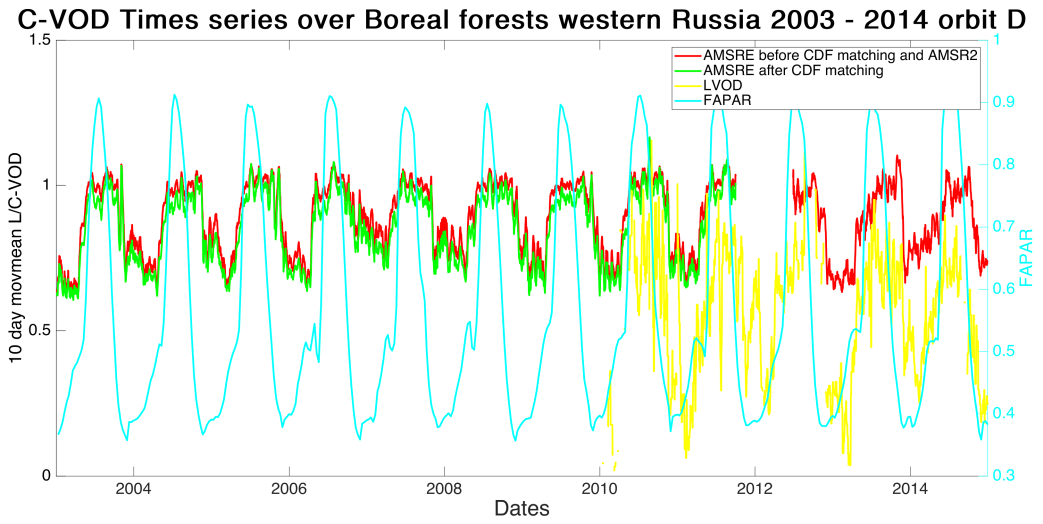

Figure 37: For the point [61° N, 44.6°E] (western Russia): 2003-2014 time series of the AMSRE/AMSR2 C-VOD before CDF matching (red), 2003-2011 time series of AMSRE C-VOD after CDF matching with AMSR2 (green), 2010-2014 time series of the SMOS L-VOD (yellow), 2003-2014 time series of FAPAR from Copernicus (cyan). The L/C-VOD time series are 10 day moving averages.

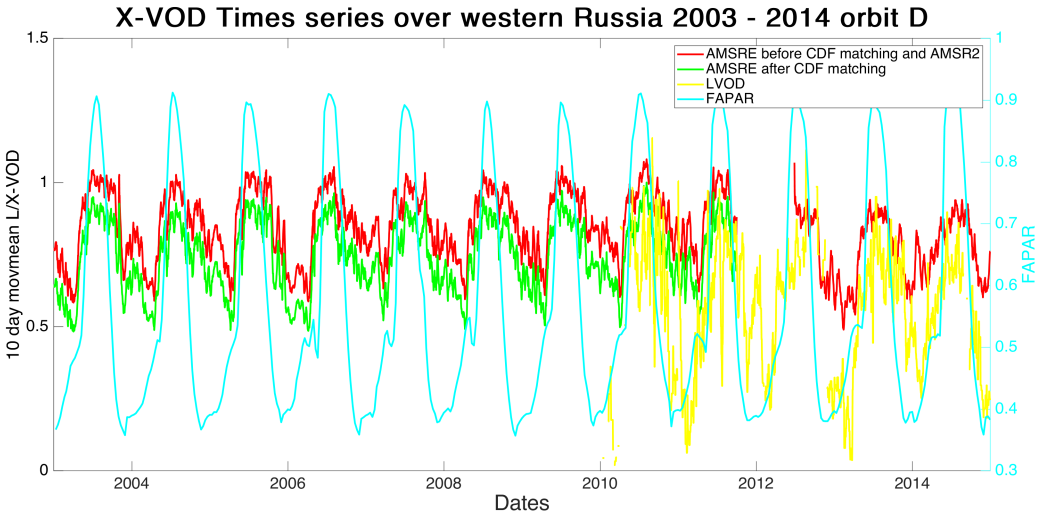

Figure 38: For the point [61° N, 44.6°E] (western Russia): 2003-2014 time series of the AMSRE/AMSR2 X-VOD before CDF matching (red), 2003-2011 time series of AMSRE X-VOD after CDF matching with AMSR2 (green), 2010-2014 time series of the SMOS L-VOD (yellow), 2003-2014 time series of FAPAR from Copernicus (cyan). The L/C-VOD time series are 10 day moving averages.

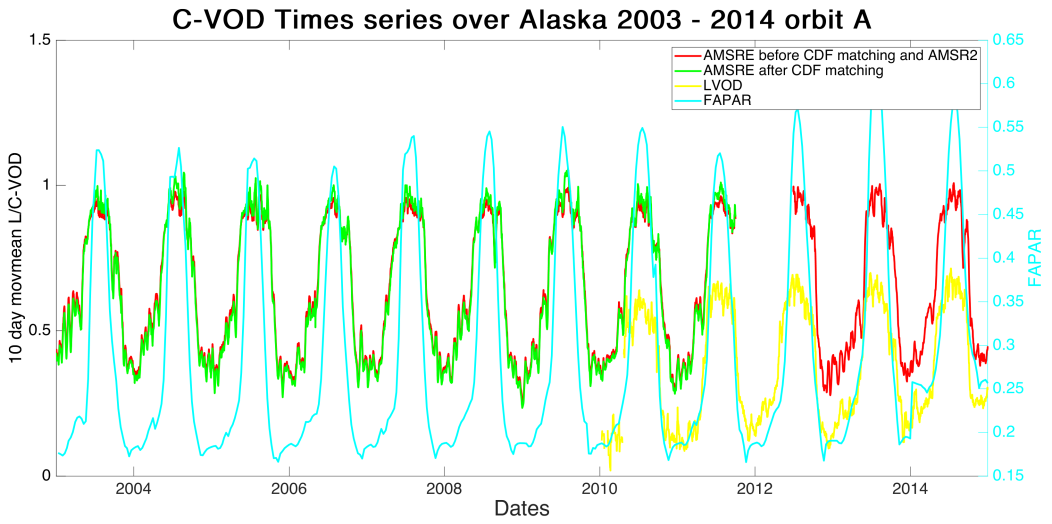

Figure 39: For the point [65.04° N, -143.19°E] (Alaska): 2003-2014 time series of the AMSRE/AMSR2 C-VOD before CDF matching (red), 2003-2011 time series of AMSRE C-VOD after CDF matching with AMSR2 (green), 2010-2014 time series of the SMOS L-VOD (yellow), 2003-2014 time series of FAPAR from Copernicus (cyan). The L/C-VOD time series are 10 day moving averages.

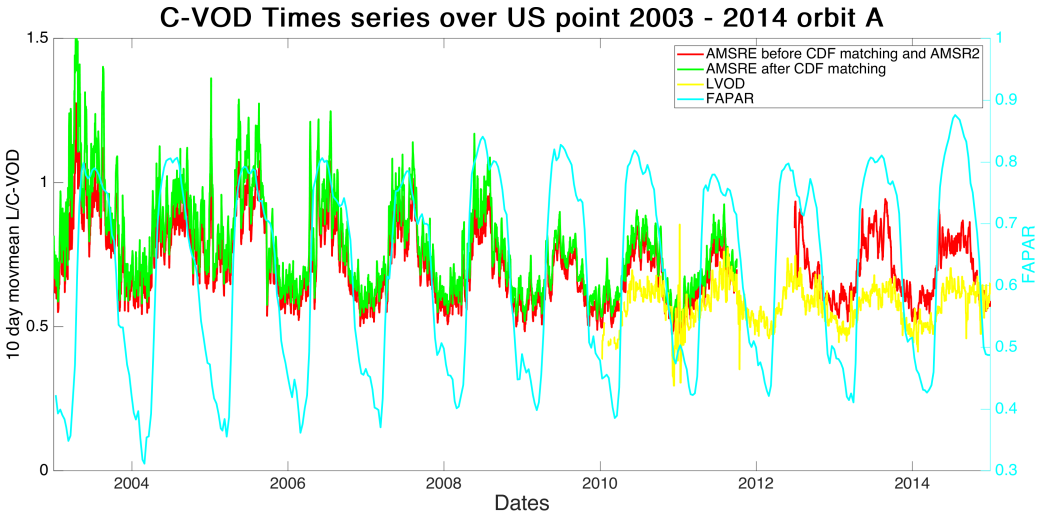

Figure 40: For the point [34.2° N, -92.5°E] (USA): 2003-2014 time series of the AMSRE/AMSR2 C-VOD before CDF matching (red), 2003-2011 time series of AMSRE C-VOD after CDF matching with AMSR2 (green), 2010-2014 time series of the SMOS L-VOD (yellow), 2003-2014 time series of FAPAR from Copernicus (cyan). The L/C-VOD time series are 10 day moving averages.

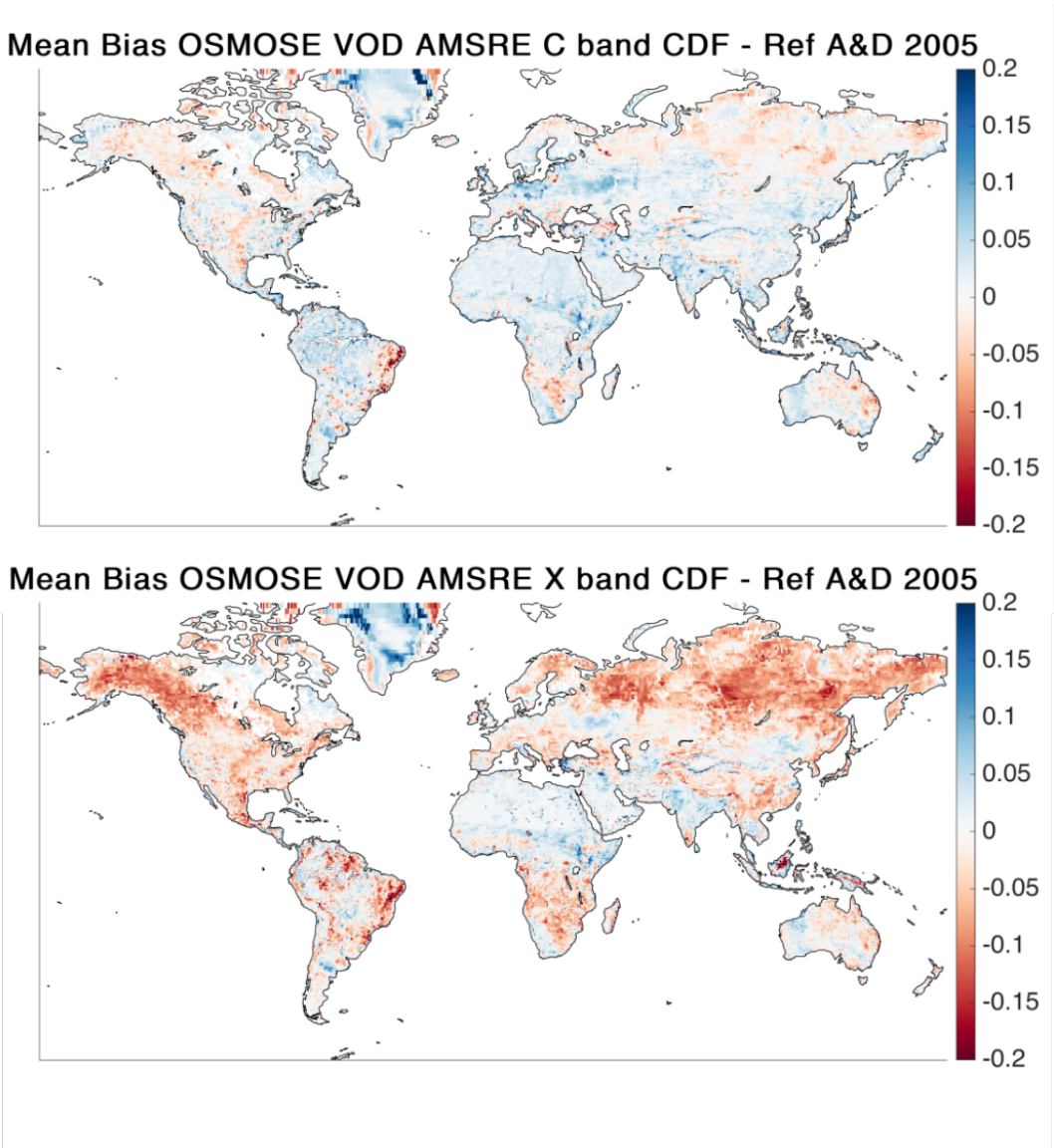

Figure 41: Yearly VOD Bias for AMSRE after minus before CDF matching for C (top) and X (bottom) band

Correction of the VOD from the AMSR sensors is mandatory. Fig. 41 shows the significant differences when applying the CDF matching correction. For our analysis, we chose to correct the AMSRE VOD, as there is no absolute method to clearly state which sensor (i.e. AMSRE or AMSR2) provides the reference TB. The correction could also have been done at the TB level as done by (22). It constitutes the most appropriate method. However, we chose to keep the "raw" VOD, so that we could perform an analysis with optical data from the datacube2. It seems that on a few nodes, the correction is not justified (as shown in Fig.39, 33 and 34). One has to keep in mind that it may be the case for other grid nodes. Both VODs (i.e. not corrected and corrected with CDF matching) are then produced and delivered for the OSMOSE project, as one can further investigate the need to apply a correction, whether on AMSRE or AMSR2 sensors.

5 Conclusion

This technical note presents the analysis of the OSMOSE VOD processed at L, C and X bands from the SMOS, AMSRE and AMSR2 sensors. These VODs are evaluated using optical data from OSMOSE datacube 2. They are then used through the OSMOSE project to compute and estimate Above Ground Biomass AGB,

which are presented and discussed in the technical note relative to the WP5 (16) and 10 of the OSMOSE project.

References

[1] Filipe Aires, Peter Weston, Patricia de Rosnay, and David Fairbairn. Statistical approaches to assimilate ascat soil moisture information—i. methodologies and first assessment. *Quarterly Journal of the Royal Meteorological Society*, 147(736):1823–1852, 2021.

[2] S. Boitard, A. Mialon, N. Rodriguez-Fernandez, J.C. Salazar Neira, and CESBIO team. OSMOSE Database Manual Microwave T3-D06 (TN03). Technical Report SO-TN-CB-GS-0115, CESBIO, Université de Toulouse, CNES/CNRS/INRAE/IRD/UT3, September 2023.

[3] S. Boitard, A. Mialon, N. Rodriguez-Fernandez, J.C. Salazar Neira, and CESBIO team. OSMOSE VOD processing chain ATBD T2-D03 (TN02). Technical Report SO-TN-CB-GS-0116, CESBIO, Université de Toulouse, CNES/CNRS/INRAE/IRD/UT3, September 2023.

[4] L. Brocca, S. Hasenauer, T. Lacava, F. Melone, T. Moramarco, W. Wagner, W. Dorigo, P. Matgen, J. Martínez-Fernández, P. Llorens, J. Latron, C. Martin, and M. Bittelli. Soil moisture estimation through ascat and amsr-e sensors: An intercomparison and validation study across europe. *Remote Sensing of Environment*, 115(12):3390–3408, 2011. URL: https://www.sciencedirect.com/science/article/pii/S0034425711002756, doi:10.1016/j.rse.2011.08.003.

[5] M. J. Brodzik, B. Billingsley, T. Haran, B. Raup, and M. H. Savoie. EASE-Grid 2.0: Incremental but Significant Improvements for Earth-Gridded Data Sets. *ISPRS International Journal of Geo-Information*, 1(1):32–45, 2012. ISSN 2220-9964. URL: http://www.mdpi.com/2220-9964/1/1/32, doi:10.3390/ijgi1010032.

[6] Mary J. Brodzik, Brendan Billingsley, Terry Haran, Bruce Raup, and Matthew H. Savoie. Correction: Brodzik, M.J., et al. EASE-Grid 2.0: Incremental but Significant Improvements for Earth-Gridded Data Sets. ISPRS International J. of Geo-Information 2012, 1, 32–45. *ISPRS International Journal of Geo-Information*, 3(3):1154–1156, 2014. ISSN 2220-9964. URL: http://www.mdpi.com/2220-9964/3/3/1154, doi:10.3390/ijgi3031154.

[7] D. Daria Malik, A. Zabukovec, and B. Berthelot. D-13 : Atbd second optical data cube. Technical Report OSMOSE-NT-024-MAG, Magellium, November 2023.

[8] D. Daria Malik, A. Zabukovec, and B. Berthelot. D-13 : Second optical data cube description. Technical Report OSMOSE-NT-006-MAG, Magellium, November 2023.

[9] D. Daria Malik, A. Zabukovec, and B. Berthelot. D-13 : Second optical data cube validation manual. Technical Report OSMOSE-NT-037-MAG, Magellium, November 2023.

[10] R. Fernandez-Moran, A. Al-Yaari, A. Mialon, A. Mahmoodi, A. Al Bitar, G. De Lannoy, N. Rodriguez-Fernandez, E. Lopez-Baeza, Y. Kerr, and J.-P. Wigneron. SMOS-IC: An Alternative SMOS Soil Moisture and Vegetation Optical Depth Product. *Remote Sensing*, 9(5), 2017. Article Number 457. URL: http://www.mdpi.com/2072-4292/9/5/457, doi:10.3390/rs9050457.

[11] Carlos M Jarque and Anil K Bera. A test for normality of observations and regression residuals. *International Statistical Review/Revue Internationale de Statistique*, pages 163–172, 1987.

[12] Hubert W Lilliefors. On the kolmogorov-smirnov test for normality with mean and variance unknown. *Journal of the American statistical Association*, 62(318):399–402, 1967.

[13] Rémi Madelon, Nemesio J. Rodríguez-Fernández, Robin van der Schalie, Tracy Scanlon, Ahmad Al Bitar, Yann H. Kerr, Richard de Jeu, and Wouter Dorigo. Toward the removal of model dependency in soil moisture climate data records by using an l-band scaling reference. *IEEE Journal of Selected Topics in Applied Earth Observations and Remote Sensing*, 15:831–848, 2022. doi:10.1109/JSTARS.2021.3137008.

[14] L. Moesinger, W. Dorigo, R. de Jeu, R. van der Schalie, T. Scanlon, I. Teubner, and M. Forkel. The global long-term microwave vegetation optical depth climate archive (vodca). *Earth System Science Data*, 12(1):177–196, 2020. doi:10.5194/essd-12-177-2020.

[15] Nemesio J Rodríguez-Fernández, Arnaud Mialon, Stephane Mermoz, Alexandre Bouvet, Philippe Richaume, Ahmad Al Bitar, Amen Al-Yaari, Martin Brandt, Thomas Kaminski, Thuy Le Toan, et al. An evaluation of smos l-band vegetation optical depth (l-vod) data sets: high sensitivity of l-vod to above-ground biomass in africa. *Biogeosciences*, 15(14):4627–4645, 2018. doi:10.5194/bg-15-4627-2018.

[16] J.C. Salazar-Neira1, S. Boitard, S. Mermoz, A. Mialon, and N. Rodríguez-Fernández. OSMOSE (PM-VOS) WP5 report. Technical Report SO-TN-CB-GS-0117, CESBIO, Université de Toulouse, CNES/CNRS/INRAE/IRD/UT3, April 2024.

[17] M. Santoro and O. Cartus. Esa biomass climate change initiative (biomass_cci): Global datasets of forest above-ground biomass for the years 2010, 2017, 2018, 2019 and 2020, v4. *NERC EDS Centre for Environmental Data Analysis*, 2023. URL: https://dx.doi.org/10.5285/af60720c1e404a9e9d2c145d2b2ead4e, doi:10.5285/af60720c1e404a9e9d2c145d2b2ead4e.

[18] Mike Schwank, Reza Naderpour, and Christian Mätzler. "tau-omega"- and two-stream emission models used for passive l-band retrievals: Application to close-range measurements over a forest. *Remote Sensing*, 10(12), 2018. URL: https://www.mdpi.com/2072-4292/10/12/1868, doi:10.3390/rs10121868.

[19] P. Waldteufel, J.-L. Vergely, and C. Cot. A modified cardioid model for processing multiangular radiometric observations. *IEEE Transactions on Geoscience and Remote Sensing*, 42(5):1059–1063, 2004. doi:10.1109/TGRS.2003.821698.

[20] Mengjia Wang, Philippe Ciais, Rasmus Fensholt, Martin Brandt, Shengli Tao, Wei Li, Lei Fan, Frédéric Frappart, Rui Sun, Xiaojun Li, Xiangzhuo Liu, Huan Wang, Tianxiang Cui, Zanpin Xing, Zhe Zhao, and Jean-Pierre Wigneron. Satellite observed aboveground carbon dynamics in africa during 2003–2021. *Remote Sensing of Environment*, 301:113927, 2024. URL: https://www.sciencedirect.com/science/article/pii/S0034425723004790, doi:10.1016/j.rse.2023.113927.

[21] Mengjia Wang, Lei Fan, Frédéric Frappart, Philippe Ciais, Rui Sun, Yi Liu, Xiaojun Li, Xiangzhuo Liu, Christophe Moisy, and Jean-Pierre Wigneron. An alternative amsr2 vegetation optical depth for monitoring vegetation at large scales. *Remote Sensing of Environment*, 263:112556, 2021.

[22] Mengjia Wang, Jean-Pierre Wigneron, Rui Sun, Lei Fan, Frédéric Frappart, Shengli Tao, Linna Chai, Xiaojun Li, Xiangzhuo Liu, Hongliang Ma, Christophe Moisy, and Philippe Ciais. A consistent record of vegetation optical depth retrieved from the amsr-e and amsr2 x-band observations. *International Journal of Applied Earth Observation and Geoinformation*, 105:102609, 2021. URL: https://www.sciencedirect.com/science/article/pii/S0303243421003160, doi:10.1016/j.jag.2021.102609.

[23] J.-P. Wigneron, T.J. Jackson, P. O'Neill, G. de Lannoy, P. de Rosnay, J.P. Walker, P. Ferrazzoli, V. Mironov, S. Bircher, J.P. Grant, M. Kurum, M. Schwank, J. Munoz-Sabater, N. Das, A. Royer, A. Al-Yaari, A. Al Bitar, R. Fernandez-Moran, H. Lawrence, **A. Mialon**, M. Parrens, P. Richaume, S. Delwart, and Y. Kerr. Modelling the passive microwave signature from land surfaces: A review of recent results and application to the L-band SMOS and SMAP soil moisture retrieval algorithms. *Remote Sensing of Environment*, 192:238 – 262, 2017. URL: http://www.sciencedirect.com/science/article/pii/S0034425717300366, doi:10.1016/j.rse.2017.01.024.

[24] Y. Zhou and M. Schwank. THEORETICAL ANALYSIS OF MULTI-FREQUENCY VOD AND ALBEDO T1-D02 (TN01). Technical Report TN_PM-VO-S_WP1, WSL, June 2020.

[25] R.-M. Zotta, L. Moesinger, R. van der Schalie, M. Vreugdenhil, W. Preimesberger, T. Frederikse, R. de Jeu, and W. Dorigo. Vodca v2: Multi-sensor, multi-frequency vegetation optical depth data for long-term canopy dynamics and biomass monitoring. *Earth System Science Data Discussions*, 2024:1–45, 2024. URL: https://essd.copernicus.org/preprints/essd-2024-35/, doi:10.5194/essd-2024-35.